

Assessing land use and land cover dynamics using composites of spectral indices and principal component analysis: A case study in middle Awash subbasin, Ethiopia

Zebene Lakew Teffera^{**}, Jianhua Li*, Tsega Mengesha Debsu, Belayneh Yigez Menegesha

UN-Environment-Tongji Institute of Environment for Sustainable Development, College of Environmental Science and Engineering, Tongji University, Shanghai 200092, China

ABSTRACT

As of recent decades land use and land cover (LULC) change studies have received much attention partly because of the global effect on climate change and mainly because of the local effect on the health and sustainable provision of ecosystem services. Nonrenewable resources are deteriorating from time to time due to the coupled pressure from population growth and global climate change. Monitoring LULC dynamics and setting appropriate management plans have become crucial, which required timely and accurate information. In order to predict future LULC change impacts and simultaneously fulfill daily demand of the growing population, land use planners and policy makers require accurate information on regular basis. Since the last couple of decades application of remote sensing for earth resource management has become popular and a number of earth observation satellites have been developed and launched to the space to collect land resource data of varied temporal and spatial resolution. The knowledge level to interpret these data have also increased and helped to monitor ecosystem structure and its health status at low cost and less effort. In this study we have employed remote sensing and GIS techniques integrating with ground information to analyze LULC dynamics in Middle Awash subbasin from year 1995 to 2017. Eight different spectral indices were algebraically calculated and best composites were used for land feature identification. Principal component analysis (PCA) has also helped to extract the most useful spectral information by compressing redundant data embedded in each spectral channel. The result has greatly assisted to easily identify and trace training polygons for machine learning processes. An overall classification accuracy of 91.8% with kappa coefficient of 0.89 was achieved after applying the aforementioned techniques based on the chosen maximum likelihood supervised image classification algorithm. The change detection analysis has revealed that Middle Awash subbasin has undergone a significant change, which is attributed mainly to anthropogenic activities. Lake Beseka has expanded along with the expansion of irrigation development in the subbasin creating environmental, social and economic impacts. This study has depicted the importance of compositing spectral indices for better classification accuracy. It has also highlighted the current status of the subbasin from which policy makers could extract basic information for policy amendments.

1. Introduction

Fulfilling demands of the rapidly growing population without affecting the sustainability of ecosystem services are the main interest and concern of the current world (Galvani, Bauch, Anand, Singer, & Levin, 2016). Poverty is a severe challenge of developing nations where African countries, particularly East African countries including Ethiopia, have still remained suffering from food and nutrition security problems at most (Gebrehiwot & van der Veen, 2014). To cope with food shortage problems and to fulfill daily demands, people

continuously interact with their environment inducing pressure beyond ecosystem carrying capacity. A number of developmental sectors, which intensively require ecosystem services have been emerged constraining and challenging sustainability of ecosystem services. Irrigation development is among the rapidly growing sectors with positive impact in terms of ensuring food security, stabilizing crop prices and contributing its share towards minimizing terrestrial carbon emission. Nonetheless, it challenges the sustainability of future water security unless appropriate policy is set for efficient water utilization (Liu et al., 2017b).

* Corresponding author.

** Corresponding author.

E-mail addresses: zebenelakew@tongji.edu.cn (Z.L. Teffera), leejianhua@tongji.edu.cn (J. Li).

Moreover, degradation of environmental resources is further aggravated by climate change resulting in socio-economic instability and population displacement (Warner, Hamza, Oliver-Smith, Renaud, & Julca, 2009). The joint effect of anthropogenic activity and climate change alters the natural state of the environment and shapes the traditional landscapes (Brunori, Salvati, Mancinelli, Smiraglia, & Biasi, 2016). Agricultural expansion, land use policies and environmental calamities like drought and flooding are always exerting pressure on the environment resulting in land use and land cover (LULC) changes. There are a number of disturbance sensitive ecosystem setups like wetlands, flood plains, wildlife habitats, desert fringes, recreational sites, world heritage sites, energy development and production areas, residential and industrial development areas, which need accurate information for timely policy adjustments and remedial measures (Abdulaziz, Hurtado and Al-Douri, 2009; Anderson, Hardy, Roach, & Witmer, 2001; Michel et al., 2013; Zhou et al., 2010). In order to curb these interrelated problems and to support evaluation of the status and transition of ecosystems, monitoring and mapping land cover changes with reliable information are extremely important (Jin, Yang, Zhu, & Homer, 2017; Mushore, Mutanga, Odindi, & Dube, 2016). Simulating future changes is also important to understand the degree of interaction between human beings and their environment and to devise appropriate counteractive remedial measures (Pathak, 2014). Studies have shown that some developing countries could wisely reconcile environmental degradation: for example minimizing deforestation while improving agricultural production by establishing sound policy and problem solving innovations (Lambin & Meyfroidt, 2011). Ecological water diversion project in China has proved the feasibility of restoring degraded vegetation, improving soil condition and raising groundwater level (Bao, Huang, Ma, Guo, & Wang, 2017). The role of protected areas in conserving biodiversity and maintaining the integrity of an ecosystem was well represented by the work of Sieber et al. (Sieber et al., 2013). These facts generally depict that monitoring ecosystem disturbances using accurately retrieved data is important to develop change predictive models, devise appropriate corrective measures and secure environmental, social and economic sustainability of the entire ecosystem (Alphan, Doygun, & Unlukaplan, 2009; Hilker et al., 2009).

Monitoring environmental status and analyzing LULC change trends using remote sensing techniques have become popular these days owing to the technological advances in the earth observation system and their availability at different costs depending on data quality and mission of data providers (Feng et al., 2017; Kamh, Ashmawy, Kilias, & Christaras, 2012; Li et al., 2017; Roy et al., 2016; Vogelmann, Gallant, Shi, & Zhu, 2016). Opportunities have been created by institutions dedicated to earth resource studies like the United States Geological Survey (USGS), which started releasing moderate and medium resolution multispectral imagery dataset free of charge from their over forty years Landsat archives on regular basis. Landsat imageries are of special interest for their historical time series data and their suitability for large catchments LULC change detection studies (Wulder et al., 2008) and also for analyzing effects of natural disasters and recovery rates through the use of different image processing algorithms (Wagner, Myint, & Cerveny, 2012). Developing countries, which cannot afford allocating adequate financial resources for ground survey and monitoring programs are taking full advantage of accessing and utilizing these freely available imagery datasets, particularly for studies related to rapidly changing large catchments like that of Middle Awash subbasin of Ethiopia.

Despite the freely available moderate and medium resolution imageries, there are still challenges of converting the embedded data to useful information. The first challenge is associated with problems of acquiring cloud free imageries at the satellite's revisit times. This restricts the analyses of land surface change trends in reflectance over time to cloud-free imageries (Goodwin, Collett, Denham, Flood, & Tindall, 2013). Fortunately, a good opportunity of acquiring Landsat imageries in 8 days interval was created during the periods between the

launch of Landsat-7 in April 15, 1999 and official decommissioning of Landsat-5 in June 05, 2013. The continuity has been again maintained after the launch of Landsat-8 in 2013, which offers 16-day repetitive earth coverage, an 8-day repeat with Landsat-7 offset. However, Landsat-7 data quality has been degraded since May 31, 2003 after the sensor permanently lost its scan line corrector (SLC) that resulted in loss of about 20% of the data from each scene (Abd El-Kawy, Rød, Ismail, & Suliman, 2011; Gao et al., 2017). The missing data could, however, be filled by data gap filling algorithms with acceptable errors. The other major challenge is to spectrally distinguish land features having similar signatures in heterogeneous landscapes. Under this condition image classification accuracy could likely be diminished and subsequently change detection capacity would greatly be hampered due to errors induced while training a machine for classification.

In order to overcome these two big challenges a number of research works have been carried out and different techniques have been proposed in the literature. Data fusion technique was among the proposed techniques to improve temporal and spatial resolutions by blending two images with varying temporal and spatial resolutions (Gao et al., 2017; Qu, Li, & Dong, 2018). The method explores the possibility of extracting better information (either temporally or spatially) from different sensors with varying resolutions. This technique worked well in landscapes covered by well clustered homogenous land feature (Hilker et al., 2009). The challenge, however, persisted in areas covered by heterogeneous land features because of the fact that the images were again of coarse spatial resolution. Studies have also been conducted on image segmentation, which have yielded satisfactory result in areas covered by clusters of homogenous land covers: for example in the study of mapping desert buffelgrass (Brenner, Christman, & Rogan, 2012). This method, however, is still challenged by heterogeneity of land covers that degrades its applicability outside the spatial domain. Maxwell and Warner (Maxwell & Warner, 2015) have alternatively attempted combining of ancillary data from historical records and digital elevation models with image data and as a result they have obtained a better classification accuracy.

Alternatively, several studies have demonstrated the possibility of utilizing spectral indices developed from remotely sensed data as a proxy for biophysical representations of an ecosystem. In this regard, a number of research works have been carried out on vegetation related studies and a wide range of vegetation indices have been developed including the normalized difference vegetation index (NDVI), enhanced vegetation index (EVI), normalized difference greenness index (NDGI), radar vegetation index (RVI), leaf area index (LAI), coupled vegetative urban index (CVUI), soil-adjusted vegetation index (SAVI) and fractional vegetation coverage (FVC) (Bao et al., 2017; Gao, 1996; Wagner et al., 2012; Zhu et al., 2016). NDVI has received greater popularity and widely used not only for vegetation detection, but also for analysis of climate variation, human activities, and environmental events (Chen et al., 2004). NDVI is especially useful in identifying crops in irrigated fields by considering the phonological information based on cropping calendar (Akhtar, Awan, Tischbein, & Liaqat, 2017). Normalized difference water index (NDWI) and modified normalized difference water index (MNDWI) are indices proposed primarily for the analysis of water resources data and estimation of turbidity level on water bodies (Gao, 1996; McFeeters, 1996; Xu, 2006). Besides water resources study, Gao (Gao, 1996) has also demonstrated the applicability of NDWI for analysis of liquid water content of vegetation canopies.

In the indices-based multispectral image classification approach classification of built-ups and bare lands are extremely difficult due to heterogeneity and spectral similarity of both land features (Li et al., 2017). In order to minimize this challenge a lot of spectral indices have been developed, among which the following can be listed as an example: normalized difference built-up index (NDBI), enhanced built-up and bareness index (EBBI), urban index (UI), normalized difference bareness index (NDBai), and bare soil index (BI) (As-syakur, Adnyana, Arthana, & Nuarsa, 2012; Chen, Zhao, Li, & Yin, 2006; He, Shi, Xie, &

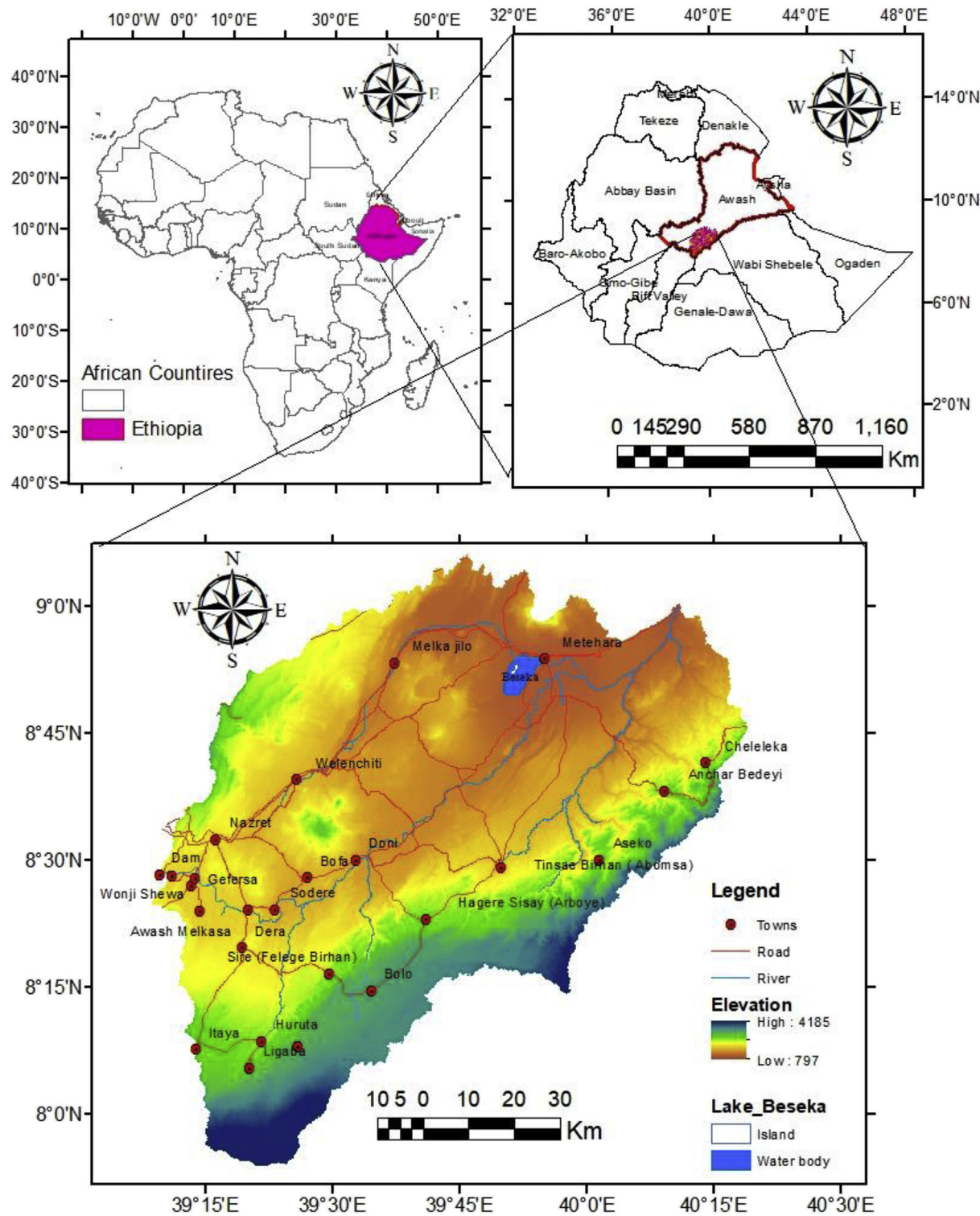


Fig. 1. Location map showing Middle Awash subbasin with respect to Africa and Ethiopia.

Zhao, 2010; Rikimaru & Miyatake, 1997; Zha, Gao, & Ni, 2003).

As it can be clearly noted from the above explanations each spectral index gives more emphasis towards separation of the particular land feature under consideration. In fact, all indices give clue about the presence of other land features based on cautiously classified threshold values. What matters in any classification attempt is that how much accurate the classification output is and its implication on LULC change detection analysis, especially vital for classifications performed based on digitally complex remotely sensed data (Congalton, 1991). Performance of any classification

technique is judged based on results of accuracy assessment. Kamh et al. (2012) have evaluated the performances of five change detection techniques: image differencing, image rationing, image overlay, multi-date principal component analysis (PCA) and post-classification comparison where the last method yielded the most satisfactory classification accuracy. This entails that caution has to be taken before applying any image classification technique and change detection method. The good thing of course is that there is an uninterrupted academic research effort to improve image classification accuracy along with the advances in acquiring

Table 1

Landsat sensors used in this study and their band distribution on the Spectrum.

Landsat 8 (OLI & TIRS)		Landsat 7 (ETM +)		Landsat 5 (TM)	
Band description	Wavelength (μm)	Band description	Wavelength (μm)	Band description	Wavelength (μm)
Band 1 — Ultra blue	0.43–0.45	Band 1 — Blue	0.45–0.52	Band 1 — Blue	0.45–0.52
Band 2 — Blue	0.45–0.51	Band 2 — Green	0.52–0.60	Band 2 — Green	0.52–0.60
Band 3 — Green	0.53–0.59	Band 3 — Red	0.63–0.69	Band 3 — Red	0.63–0.69
Band 4 — Red	0.64–0.67	Band 4 — NIR	0.77–0.90	Band 4 — NIR	0.76–0.90
Band 5 — NIR	0.85–0.88	Band 5 — SWIR1	1.55–1.75	Band 5 — SWIR1	1.55–1.75
Band 6 — SWIR1	1.57–1.65	Band 7 — SWIR2	2.09–2.35	Band 7 — SWIR2	2.08–2.35
Band 7 — SWIR2	2.11–2.29	Band 8 — Pan	0.52–0.90		
Band 8 — Pan	0.50–0.68				
Band 9 — Cirrus	1.36–1.38				
Band 10 — TIR	10.60–11.19	Band 61 — TIR	10.40–12.50 (high gain)	Band 6 — TIR	10.40–12.50
Band 11 — TIR	11.50–12.51	Band 62 — TIR	10.40–12.50 (low gain)		

remotely sensed data. Complementary to the above-mentioned single spectral index-based classification accuracy improvement efforts, the use of tasseled cap, PCA, fuzzy c-means clustering (FCMC), possibilistic C-Means (PCM) and artificial neural networks, which employ synthetic bands have been tested by many researchers (Ganbold & Chasia, 2017; Novelli et al., 2016; Sun, Huang, Cheung, Liu, & Huang, 2005). The role of the synthetic bands is to maximize dimensions in addition to the raw spectral bands for better image extraction and pattern recognition. Novelli et al. (2016) have for example proposed artificial neural network based on Landsat image to extract impervious pixels with improved classification accuracy using synthetic bands generated from PC, Tasseled Cap (TC), Brightness Temperature (BT) and vegetation indices. The work by Mello et al. (2013) was unique in effect that the proposed technique, Spectral-Temporal Analysis by Response Surface (STARS), utilized all the spectral and temporal information to represent the spectral variation over time. Unlike other applications such as PCA, whose performance depends on the nature of data distribution (requiring normal distribution), STARS performs well in any type of distribution (Mello et al., 2013). In this regard, improving pattern recognition by adding a suitable dimension without computational complexity is an ongoing research area and was also our prime motive for this research.

In Ethiopia several studies on image classification methodologies and LULC dynamics have been carried out linking with social, economic, and climatological drivers (Ariti, van Vliet, & Verburg, 2015; Biazin & Sterk, 2013; Kindu, Schneider, Teketay, & Knoke, 2015; Wondie, Schneider, Melesse, & Teketay, 2011). In this particular study we have intensively explored the possibility of improving multispectral satellite image classification accuracy by composing selected spectral indices and applying PCA in the process of investigating LULC change dynamics from year 1995 up to 2017 and future trends in Middle Awash subbasin, Ethiopia. This particular subbasin was chosen for its representativeness to complex geomorphological setup, intense anthropogenic interferences such as: irrigation development and industrial effluents, water stressed and environmentally sensitive catchment. The subbasin has been subjected to a number of developmental stresses where spatial and temporal changes along with their associated impacts have not been well studied yet. This study partially addressed these issues by investigating the change dynamics occurred in the specified time period applying the proposed classification and change detection techniques supported by software packages developed for remote sensing and geographic information system (GIS) analysis.

2. Study area and data

2.1. Study area

The study area is located in the main Awash River basin between latitude 7°53'50.42"N - 9°6'3.92"N and longitude 39°8'0.55"E - 40°19'2.79"E with an estimated total area of about 9,517 km² (Fig. 1). It

is part of the main Ethiopian Rift (MER) that stretches from the outlet point at Awash 7 kilo hydro gauging station to upstream until the outlet of Koka dam, a dam initially built for hydroelectric power generation and later with a supplementary function for irrigation development and flood control. The general Physiographic setup of the study area is characterized by plateau, rift escarpments and rift floor. It is affected by recent volcanic episodes, which occurred from Oligocene to Quaternary periods (WoldeGabriel, Aronson, & Walter, 1990). These recent geological processes have controlled the geomorphology, lithological stratification and rate of soil development. The eastern and western rift escarpments have a steep to gentle gradient with thin and less developed soils. On the other hand, the central part (rift floor) is a mixture of barren lands, volcanic domes and cones, partly undulating and more of plain surface with fertile soil, where most of the irrigation development and rain-fed agricultural activities are intensively taking place with their positive and negative impacts on the people and entire biodiversity of the subbasin. A saline and expanding lake called "Lake Beseka" occupies the largest surface area among the available water bodies (Dinka, 2017), and its expansion has become a major environmental and social concern in the subbasin (Dinka, Loiskandl, & Ndambuki, 2015).

Majority of the study area is categorized by semi-arid and arid climatic zones, with sub-humid climate at the flanking plateaus. The entire Awash basin is generally influenced by the position of the regional Inter-Tropical Convergence Zone (ITCZ), which marks the convergence of dry tropical easterlies and the moist equatorial westerlies. ITCZ reaches the study area in March from the southern direction bringing light rain. Around June it reaches the northern end, which results in the biggest summer rain. Then it goes back to the southern direction restoring the drier easterly air streams and repeats its cycle in the same fashion. Besides the influence of the ITCZ, the amount of rainfall at the highland plateau and escarpment areas is highly influenced by orographic effect and varies with change in elevation. The annual rainfall shows great variation within the subbasin following the variation in elevation that ranges from 764 m to 4185 m above mean sea level. Accordingly, lowlands with elevation lower than 1000 m above mean sea level receive annual rainfall between 400 mm and 600 mm, whereas those areas located at higher than 1000 m above mean sea level receive annual rainfall up to 1200 mm. The subbasin, in general, has a bimodal rainfall distribution pattern receiving the major rainfall from July to September and minor rainfall between March and April (Dinka, 2017).

According to the meteorological data obtained from National Meteorological Agency of Ethiopia, the maximum and minimum temperature of the subbasin was recorded in the months of June and December with around 36 °C and 13 °C respectively. The annual mean relative humidity varies between 30% and 60% having annual mean sunshine of about 8 h per day. It was also observed that temperature has a significant correlation with elevation that has resulted in an elevated evaporation rate in the lowland parts of the subbasin, with a long-term

Table 2

Metadata of images used in this study.

Date acquired	Satellite	Sensor ID	WRS Path/Row	Reflective Grid cell size (m)	Sun elevation (degree)
1995-01-14	Landsat 5	TM	168/054	30	40.75312220
1995-01-23	Landsat 5	TM	167/054	30	41.11441515
2000-02-05	Landsat 7	ETM +	168/054	30 ^a	50.57314169
2000-03-09	Landsat 5	TM	167/054	30	52.89501187
2005-01-10	Landsat 7	ETM +	167/054	30 ^a	47.35747260
2005-02-02	Landsat 7	ETM +	168/054	30 ^a	49.56773380
2010-01-15	Landsat 7	ETM +	168/054	30 ^a	47.99051193
2010-02-01	Landsat 5	TM	167/054	30	49.68984939
2015-01-06	Landsat 7	ETM +	167/054	30 ^a	48.83220375
2015-01-29	Landsat 7	ETM +	168/054	30 ^a	50.70091629
2017-01-03	Landsat 8	OLI_TIRS	167/054	30 ^a	49.07281745
2017-01-10	Landsat 8	OLI_TIRS	168/054	30 ^a	49.22584293

^a Grid cell size of the panchromatic band is 15 m.

average annual evaporation of 2485 mm as compared to the low annual precipitation of 543.7 mm (Dinka et al., 2015).

2.2. Data

A total of 9 Advanced Spaceborne Thermal Emission and Reflection Radiometer (ASTER) Global Digital Elevation Model (GDEM) tiles were used for project area delineation and terrain processing. The acquired ASTER GDEM is a product of the joint Ministry of Economy, Trade, and Industry (METI) and the National Aeronautics and Space Administration (NASA), which was released in mid-October, 2011 and has a 1arc-second pixel size (approximately 30 m at equator) referenced to the 1984 World Geodetic System. All the 9 GDEM tiles used in this study were freely downloaded from <https://earthexplorer.usgs.gov/> website.

Landsat images of six years (1995, 2000, 2005, 2010, 2015 and 2017) were considered to test our proposed image classification methodology and study the LULC dynamics in Middle Awash subbasin. The study area is covered by two scenes: path/row 167/054 and 168/054. Cloud free images of similar seasons and dry period were chosen to minimize atmospheric and phonological effects respectively. These images are Landsat Collection 1 Level-1 data products of Landsat 5 Thematic Mapper (TM), Landsat 7 Enhanced Thematic Mapper Plus (ETM+) and Landsat 8 Operational Land Imager (OLI) acquired from the U.S. Geological Survey (USGS) Earth Resources Observation and Science (EROS) Center by navigating through the website: <https://glovis.usgs.gov/>. Access to all products were free of charge with the only requirement of registration for statistical analysis purpose. Details of the sensors and their band distribution as well as metadata of the selected images are presented in Tables 1 and 2 respectively.

Besides the satellite data we have collected ancillary data including thematic and topographic maps, aerial photos, land use and soil maps, hydrological and meteorological maps, infrastructural, socio-economic and administrative boundaries from different institutions (Ministry of Water Irrigation and Electricity of Ethiopia, Awash Basin Authority,

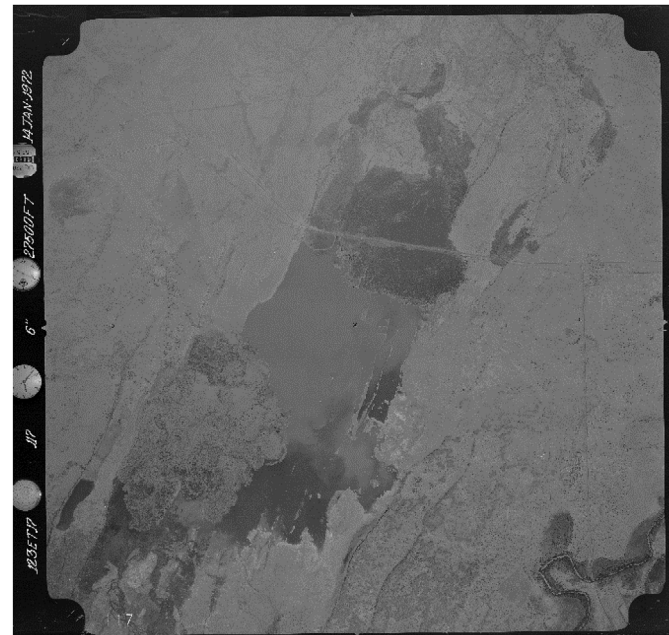


Fig. 2. One of the aerial photos taken in 1972 showing the size of Lake Beseka covering only 11 km² surface area in the same year.

National Meteorology Agency of Ethiopia and Central Statistical Agency of Ethiopia). Hand-held Garmin GPS was used for location navigation and data collection for ground truthing that would be used for orthorectification and accuracy assessment. Table 3 shows the ancillary and other supplemental data including their sources and (Fig. 2 and Fig. 3) show exemplary figures of data sources.

Table 3

Ancillary and other supplemental data sources utilized in the study.

Data type and description	Source
Aerial photos around Lake Beseka taken in 1972 from a height of 27500 feet.	Ethiopian mapping agency
Topographic map of Beseka, Melkajilo, Nura hera and Nazeret produced at a scale of 1:50,000 and 1:250,000	Ethiopian mapping agency
EthioGIS-I, produced in 1999 at country level consisting of shapefiles of watersheds, hydrology, climate, land resources, soil, administrative boundaries and infrastructures at scales ranging 1:100,000 and 1:1,000,000	Ministry of Agriculture, Addis Ababa
Ethiopia Land Cover 2003, 2008, 2013 Scheme I and II Maps produced at a scale of 1:2,250,000	Regional Centre for Mapping of Resources for Development (RCMRD)
Geospatial Information System Ethiopia (EthioGIS-II) produced in 2015, which is an update of EthioGIS 1 and scale ranging from 1:100,000 to 1:1,000,000	Water and Land Resource Centre (WLRC), Addis Ababa
Meteorological data of stations in the study area	National Meteorological Agency of Ethiopia
Hydrological data of the study area	Ministry of Water Irrigation and Electricity of Ethiopia

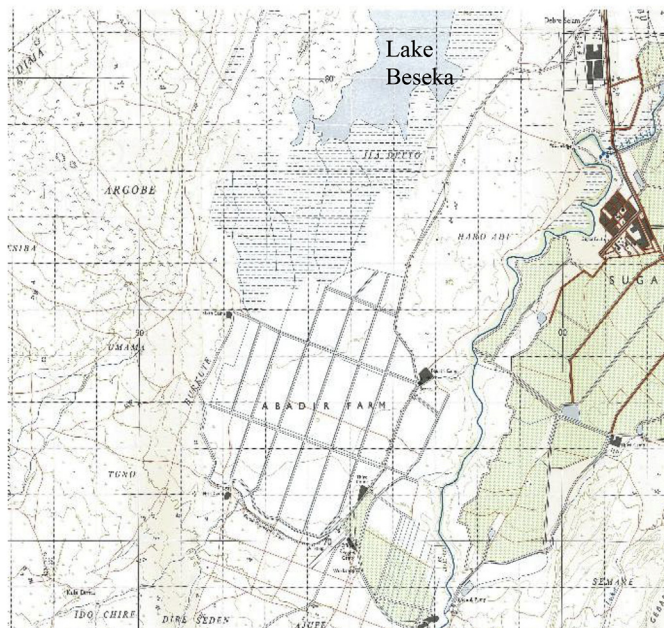


Fig. 3. Topographic map showing Metahara sugarcane at the southern and eastern edges of Lake Beseka.

3. Methods

3.1. Study area delineation

A watershed delineation approach was followed to capture all areas contributing flow to the chosen outlet point at Awash 7 kilo hydro-station. Since the acquired GDEM data were in Geographic Coordinate System and spatial analysis required planar dimension, all the 9 tiles were projected to WGS 1984 UTM Zone 37N coordinate system using ArcGIS 10.2.2 software package. All the tiles were then mosaicked into a single raster image followed by delineation of the entire catchment and sub-watersheds applying the delineation procedures included in ArcHydro tool, an add-on in ArcGIS. Because of the fact that an outlet-based delineation approach considers all the upstream watershed areas, we defined our region of interest from the generated sub-watershed polygons and subset using the clip spatial analysis tool from the geo-processing tool box.

3.2. Image pre-processing

Image pre-processing is required to obtain interpretable data that has addressed the effects of artifacts from sensor products and atmospheric interferences so as to properly distinguish land features based on their reflectivity (Chander, Markham, & Helder, 2009; Coppin, Jonckheere, Nackaerts, Muys, & Lambin, 2004). The image pre-processing work in this study was carried out using ENVI version 5.3 image processing software package. For this particular study we have limited our scope of study to Blue, Green, Red, NIR, SWIR1 and SWIR2 bands and excluded the rest of spectral channels mainly to keep consistency in spectral information among all the three Landsat sensors. We particularly excluded band 1 of OLI data because of its less importance to our study as it was mainly developed to study coastal waters and atmospheric aerosol properties.

Retrieved images were first checked for geometric errors and missing data. All images were orthorectified and projected to a coordinate system of WGS 1984 UTM Zone 37N using Transverse Mercator projection system by the data providers. It was only from images of Landsat-7 ETM + sensor, that most of the data gaps were encountered, which was due to the lost SLC as explained in Section 1.

The lost data was then estimated using data gap filling algorithm, an add-in to ENVI extension and accessed from ENVI processing toolbox. As all Landsat data are delivered in the form of DN, which are the re-scaled measure of Top of Atmospheric (TOA) radiance, they do not represent the reflective property of the surface objects (Huang et al., 2008). Thus they require conversion to TOA reflectance. Before converting the raw data obtained as DN to TOA reflectance at the sensors, dark object subtraction was carried out to remove path radiance, which is the radiant flux from the energy source (sun) that hasn't reached surface element but summed up as total radiance at the sensor so that the surface reflectance can be approximated. Then the corrected DN values were converted to at-sensor spectral radiance followed by to reflectance value based on the equations given by Chander et al. (2009). The mathematical computations were carried out by the respective algorithms embedded in ENVI 5.3. Finally, as the study area is covered by two scenes, the images with the computed reflectance value were mosaicked, smoothed using edge feathering and subset to the area of interest. Masks were built to exclude borderlines and unwanted features from region of interest. For visual interpretation a stretching technique was applied by alternatively using standard deviation and histogram matching. A final enhanced false color composite image of the year 2017, which was mosaicked and subset to the project area from two Landsat-8 (OLI) scenes is presented herein for demonstration (Fig. 4).

3.3. Testing spectral separability of land features

Middle Awash has a complex geomorphological setup and diverse LULC distribution. In order to decide the number of LULC types for our study, we have integrated knowledge of the study area through review of existing documents including topographic maps, black and white aerial photos, high resolution Google earth images and personal communications with local people. Based on ground survey and records of ground truth points using hand-held Global Positioning System (GPS) unit, ancillary data obtained from different institutions and repeated preliminary automated classification of Landsat image with varying classes using unsupervised, Iterative Self-Organizing (ISO) Data classifier, we have finally decided to consider six major LULC classes for our experiment adopting the land cover classification system developed to use for remote sensing data by Anderson et al. (Anderson et al., 2001) (Table 4). We have made some modifications on the nomenclature based on area specific study interest.

Spectral separability of the identified land features were then tested by taking samples from each class. Since the main aim at this stage was simply to see the complexity of land cover distribution in terms of spectral similarity, we didn't consider randomness. We concentrated on land cover where we were confident enough to distinguish land cover type based on results of unsupervised classification, observation during reconnaissance survey, topographic and previously produced land cover maps and visual interpretation from Google earth and raw Landsat images. Since the reconnaissance survey was made in 2017 and high resolution images were only available in recent years, we made our reference with the image of the year 2017 and took samples from the other years where land cover types remained unchanged. The delineation was made using small size polygons considering the proportion of areal coverage of each class. The delineated end members, which were created in vector file format were then converted into region of interest in order to extract spectra for each class. The spectra extraction process and statistical analysis was performed using ENVI 5.3. The area for each class was calculated from the total pixel counts where one pixel represented 30 m × 30 m. We presented here in Table 5 the statistical summary of training samples for the year 1995.

End members were plotted herein versus spectral bands with spectral variability with the marked standard deviation as shown by the error bars (Fig. 5). The main purpose of the graph was to better understand the spectral regions where surface objects showed their

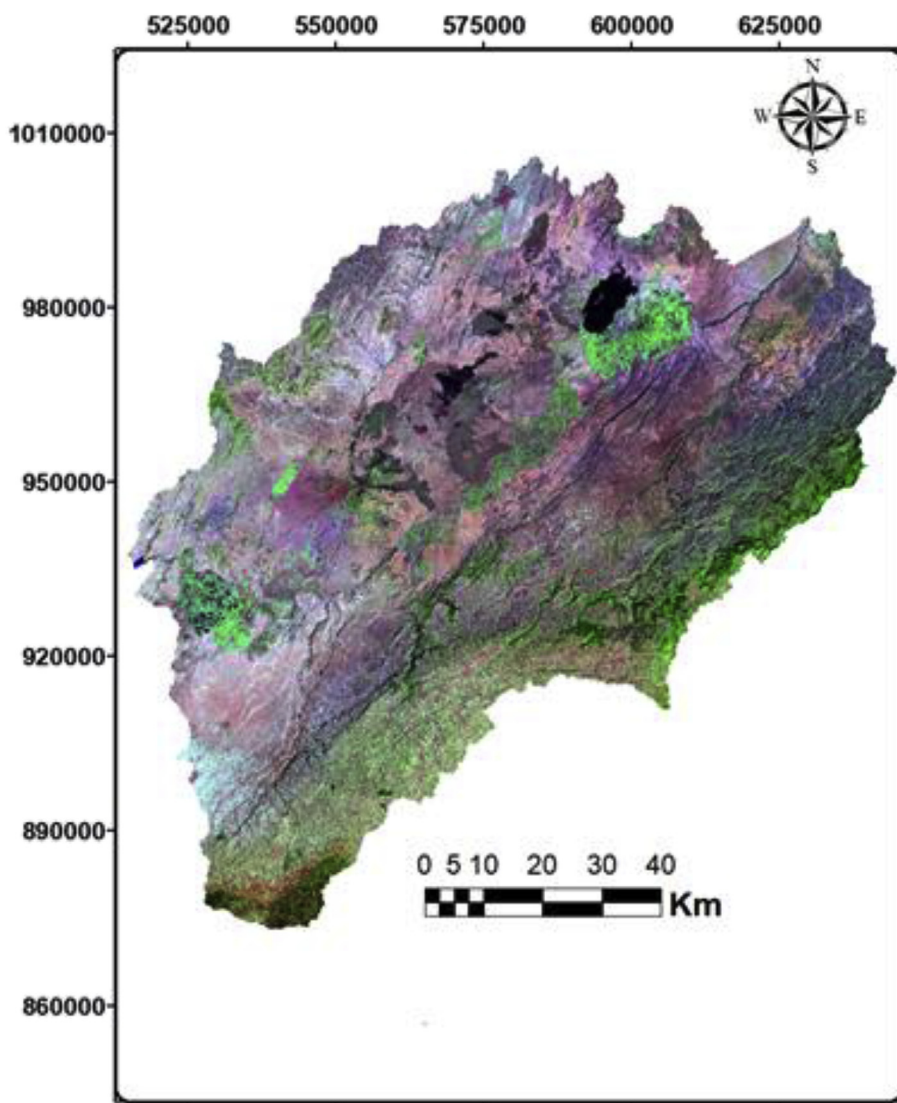


Fig. 4. A mosaicked, subset and enhanced RGB false color composite (SWIR 2, NIR, and green) from Landsat 8 OLI image acquired on January 03, 2017 and January 10, 2017. (For interpretation of the references to color in this figure legend, the reader is referred to the Web version of this article.)

signature based on their energy reflection and absorption capacity. The graph here, therefore illustrates how complex the terrain is and the importance of seeking additional techniques to discriminate one class from the other. Despite the heterogeneity of spectral responses observed from surface objects, it could be noticeable from the graph that three groups could be easily isolated based on the cumulative variability throughout the spectral ranges. The spectral signature of water body was unique that it could be easily identified from the rest of the classes. Barren/developed land and rain-fed cropland have also similar spectral properties across all spectral bands. Whereas forest, irrigated farmland and wood/shrubland similarly showed resemblance in

Table 5

Statistical summary of training samples taken for the year 1995 for spectra extraction.

Feature class	Pixel Count	Percent
Barren/developed land	17856	20.4
Forest	8456	9.7
Irrigated farmland	7564	8.6
Rain-fed cropland	23755	27.1
Water body	4565	5.2
Wood/shrubland	25428	29.0

Table 4

Identified LULC class and their description.

Class name	Class description
Barren/developed land	Consists of rock outcrops, sands, thin soil not able to support life, urban and rural settlements, buildings, constructed infrastructure like paved land surfaces and asphalt roads
Forest	Tall evergreen, deciduous and mixed forests with sufficient canopy cover
Irrigated farmland	Large scale farmland growing annual crops mainly sugarcane and citrus fruits using irrigation water diverted from rivers
Rain-fed cropland	Harvested agricultural cropland growing seasonal crops with leftover crop residues
Water body	Lakes, rivers, streams, canals and reservoirs
Wood/shrub land	Short dispersed trees, herbaceous rangelands, shrubs and brush rangelands

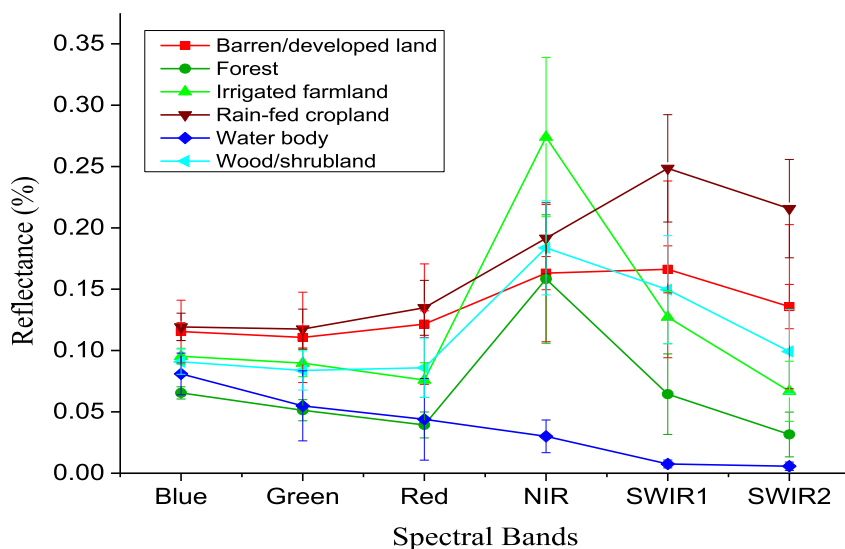


Fig. 5. Spectral representation of LULC in Middle Awash subbasin extracted from image taken from year 1995.

Table 6
Correlation matrix of spectral bands based on image of the year 1995.

Bands	Band1	Band2	Band3	Band4	Band5	Band7
Band1	1	0.96649	0.94373	0.4754	0.77917	0.85505
Band2		1	0.98307	0.61106	0.8551	0.88855
Band3			1	0.59018	0.89089	0.91681
Band4				1	0.68761	0.52448
Band5					1	0.9459
Band7						1

Table 7
Covariance matrix of spectral bands based on image of the year 1995.

Bands	Band1	Band2	Band3	Band4	Band5	Band7
Band1	0.00018	0.00024	0.00033	0.00022	0.00049	0.0005
Band2		0.00033	0.00047	0.00038	0.00074	0.00071
Band3			0.00069	0.00053	0.00111	0.00105
Band4				0.00115	0.0011	0.00078
Band5					0.00223	0.00195
Band7						0.0019

Table 8
Percent and accumulative eigenvalues of the principal components (PC) based on image of the year 1995.

PC Layer	Eigen Value	Percent of Eigen Value	Accumulative of Eigen Value
1	0.00554	85.3766	85.3766
2	0.00069	10.6675	96.0441
3	0.00019	2.9657	99.0098
4	0.00005	0.7751	99.785
5	0.00001	0.1704	99.9554
6	0	0.0446	100

spectral properties. After having clear understanding of these properties we tried to explore if spectral channels could deliver better information as a result of compressing spectral information and removing redundant data applying PCA. We further analyzed the applicability of compositing different spectral indices to obtain a better classification accuracy.

3.4. Generating principal components of spectral bands

PCA is a data reduction or compression technique, which aims at

extraction of maximum information from a dataset by removing redundant data through linear transformation in a step by step process. PCA captures the key components in a dataset, puts them in a linear space or dimensions and links the redundant information into them (Xu, Gao, & Li, 2017). It is a mathematical procedure, which reduces the number of dimensions in a dataset by transforming the original data presented in a higher dimension to a new uncorrelated lower dimension through orthogonal projection and truncation of the transformed data in three main stage: 1) covariance matrix calculation, 2) Eigen problem, and 3) data projection (Zabalza et al., 2014). The entire process involves clustering of correlated data, stretching them to consecutive axes with the first axis (PC) capturing the maximum variation. That means, the first PC or dimension contains the largest possible variance followed by the second PC capturing the variation that couldn't be captured by the first PC, which is orthogonal to the first PC. The data capturing process continues with additional PCs until all original data are fully captured, which in our case are equivalent to the number of spectral bands considered for the analysis in an iterative way. However, since the purpose of PCA is to reduce the number of dimensions by gathering the most useful information (variations) that could be captured in the first few components and colored visualization is made by the composition of three components, it is quite enough to consider the first three PCs in which more than 99% of spectral information in most Landsat images could be captured in these three PCs. The PCA algorithm, in general, maintains the content and structure of the original data, reduces noise and compacts the data by reducing the dimensionality of the independent feature space without losing class separability (Deepa & Thilagavathi, 2015; Ding, Chen, & Meng, 2018; Jimenez & Landgrebe, 1999).

In image classification and analysis process it is, therefore, the most important process as a huge amount of redundant spectral data included in different bands come along with the image files without having much object discriminatory power. It is particularly important in that unless the number of input dimensions are reduced to the optimum level, the number of training samples that has to be taken for machine learning increases exponentially with the number of input dimensions and causes degradation of the quality of the data to yield a statistically sound result (i.e. the class discriminating power of the data decreases due to noise and computational complexity). In order to facilitate the analysis process, therefore, most statistical and GIS packages have embedded PCA algorithm where users can simply apply the algorithm for their image analysis based on the required inputs. In this study we have applied the PCA algorithm built in ArcGIS 10.2.2 after

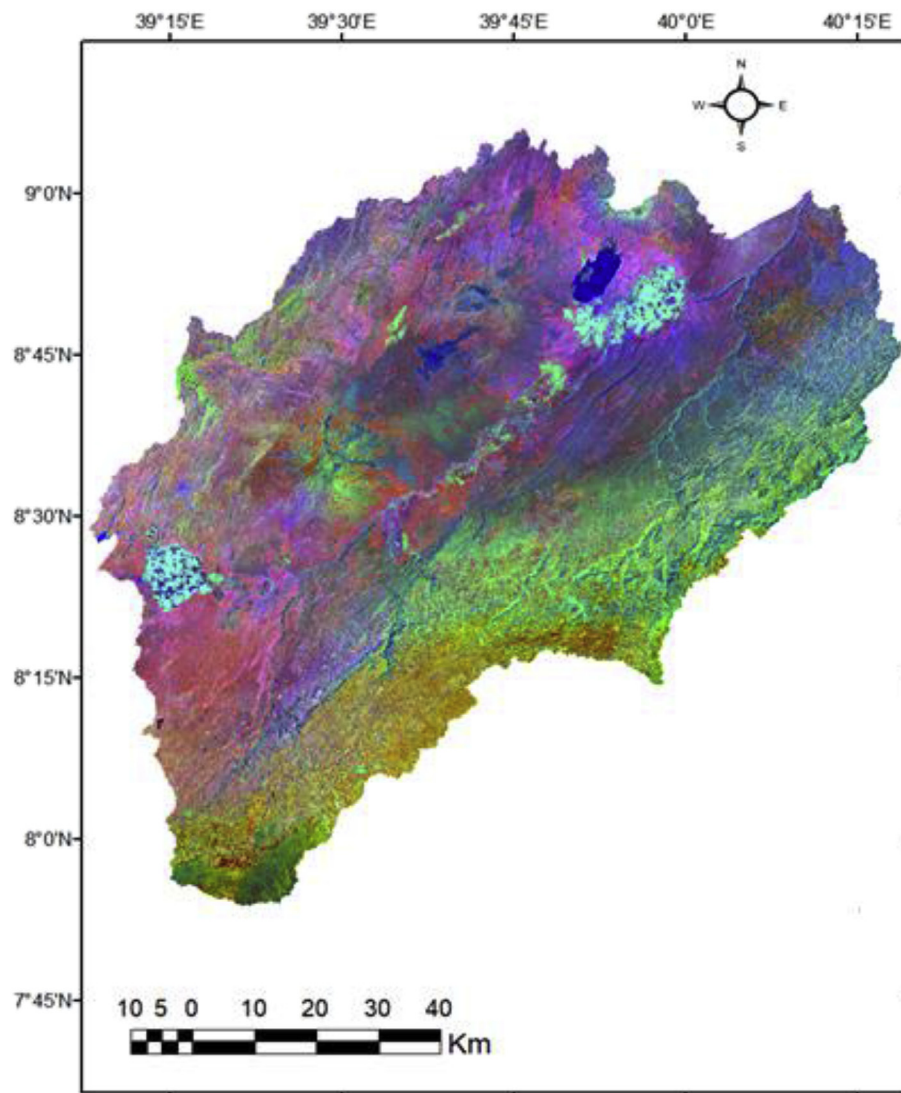


Fig. 6. Color composite map of the year 1995 TM image produced from the first three principal components. (For interpretation of the references to color in this figure legend, the reader is referred to the Web version of this article.)

pre-processing the raw Landsat image with ENVI version 5.3. The resulting output yielded three main tables: [Table 6](#), [Table 7](#) and [Table 8](#) showing the correlation matrix of spectral bands, their covariance matrix and Eigen values of principal components respectively. The PCA result revealed that there is high correlation and low covariance among spectral bands signifying the presence of redundant data in the acquired image dataset as shown in [Tables 6 and 7](#) and requiring removal of these redundant data. The Eigen values in [Table 8](#) represent the total amount of variation that could be extracted by each PC layer. The first three PC layers could explain more than 99% of the variation with the first PC explaining 85.4% of the variation in the dataset followed by the second and third PCs with 10.6% and 3% respectively. It is therefore, evident that there wouldn't be much loss of data by dropping the remaining PC layers, rather it could minimize computational complexity and remove unnecessary noise. Hence, we have utilized the first three PCs to make a color composite map, which helped to trace training polygons that were used to train a machine for supervised-based image classification algorithm. The same procedure was followed for all of the six years' images and thus, we presented herein the color composite of the three PCs taken from image of the year 1995 ([Fig. 6](#)).

3.5. Spectral indices computation and categorization

A total of eight potential indices were selected for this study and their values were computed using band algebra applying the expressions stated in [Equation \(1\) through \(8\)](#). Reflectance values at the selected band region were used to apply the algebraic expressions in the raster calculation. The output of each index was then classified using natural breaks classification algorithm. A graduated color from deep red to deep green was applied in a descending order, where the highest figure with deep red color depicting pixels of land features to be identified by the spectral index under consideration ([Fig. 7](#)). The rationale behind using natural breaks for spectral indices classification was that natural breaks could best approximate potential class boundaries and are good guides to locate the demarcation threshold values. The graduated colors were chosen in order to have a consistent change of values from deep red to deep green in a descending order as each index was developed by the developers to amplify the targeted land cover with the highest value and it gives opportunity to classify other surface objects based on cautiously identified threshold values. However, for the classification purpose we have used ground reference data to select training and testing data to identify the minimum and maximum values of spectral indices for the given land cover type.

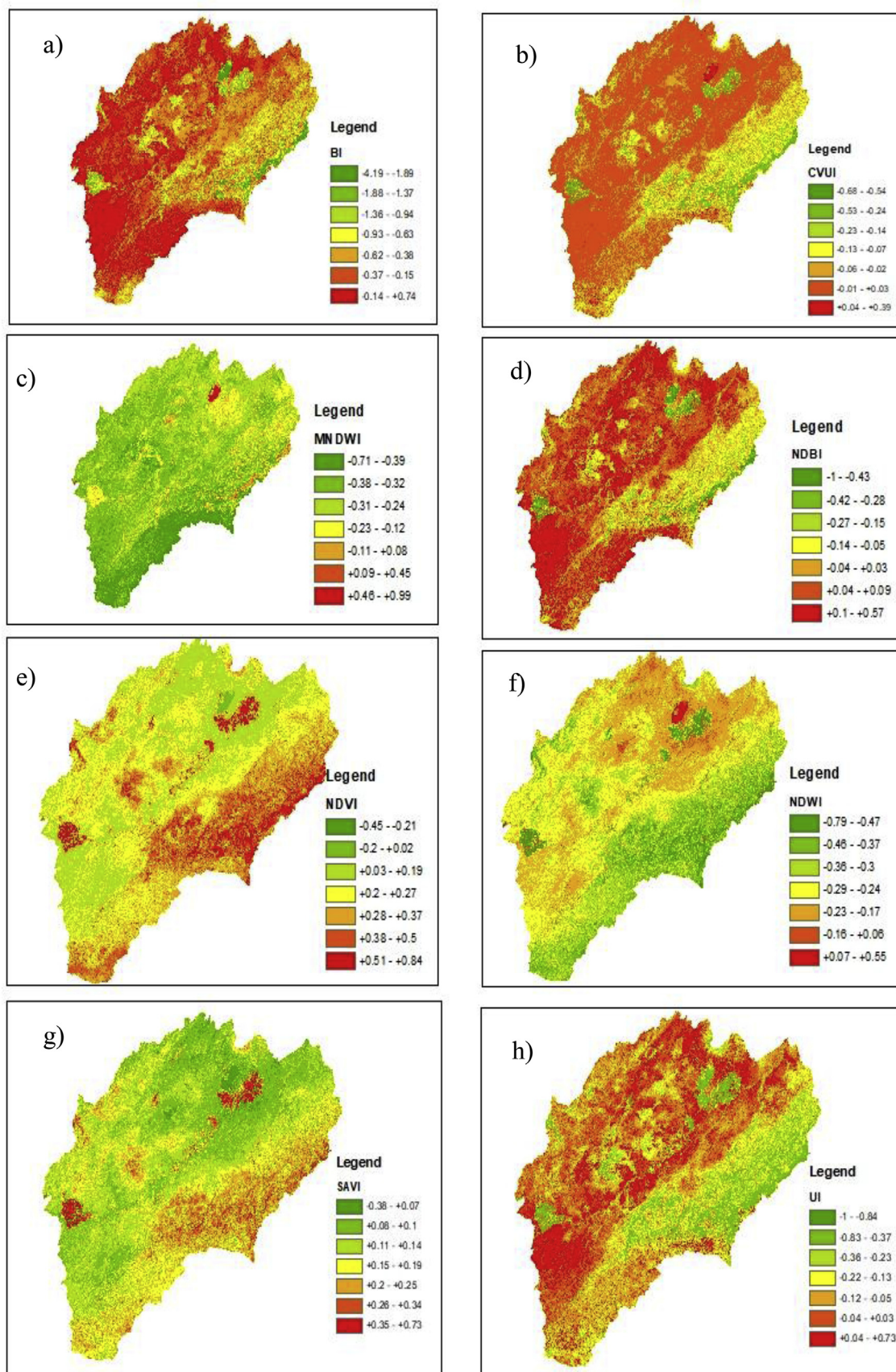
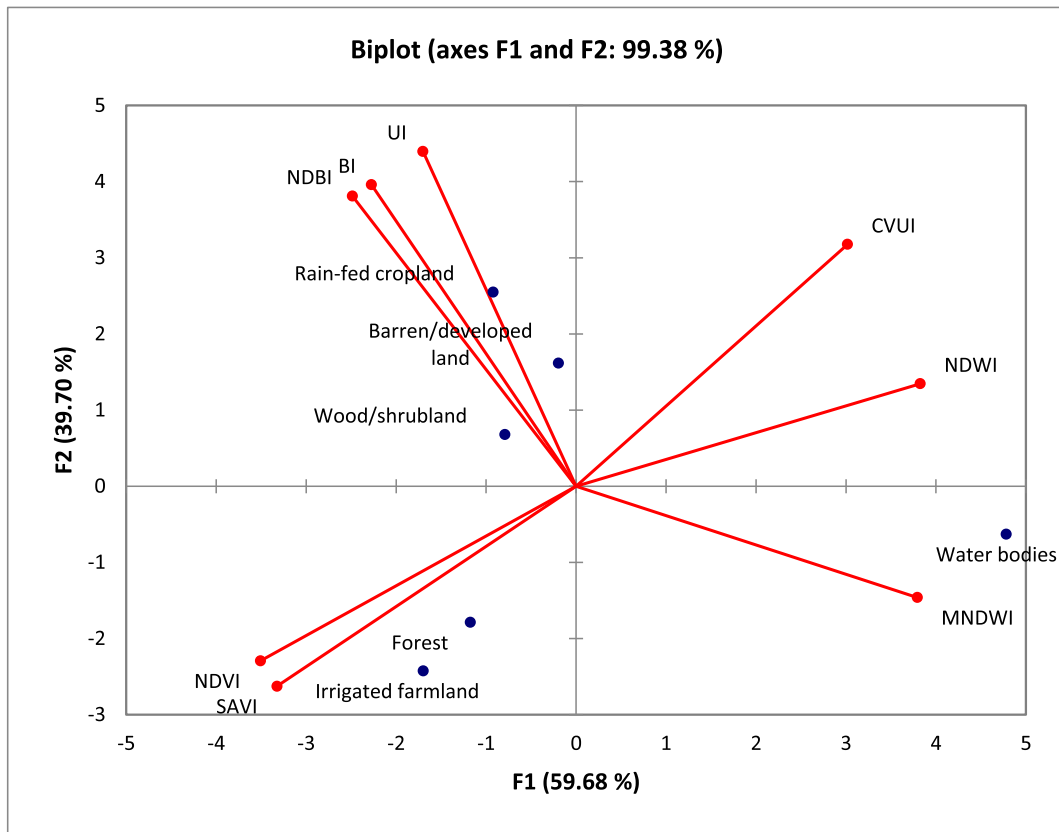


Fig. 7. Spectral indices: Group-1 (e and g); Group-2 (a, b, d and h); and Group-3 (c and f) based on image of the year 1995.

Table 9

Pearson correlation matrix for the computed spectral indices of Barren/developed class.

Variables	UI	SAVI	NDWI	NDVI	NDBI	MNDWI	CVUI	BI
UI	1	-0.132	-0.162	-0.045	0.971	-0.677	0.258	0.967
SAVI		1	-0.947	0.980	0.097	-0.628	-0.982	0.055
NDWI			1	-0.977	-0.385	0.834	0.906	-0.323
NDVI				1	0.186	-0.701	-0.973	0.115
NDBI					1	-0.830	0.034	0.985
MNDWI						1	0.526	-0.781
CVUI							1	0.097
BI								1

**Fig. 8.** Biplot of spectral indices and associated class categorization from the first two PCs based on image of the year 2017.

$$CVUI = \frac{(SWIR\ 2 - NIR) * (NIR - Red)}{(SWIR\ 2 + NIR) * (NIR + Red)}$$

$$NDVI = \frac{(NIR - Red)}{(NIR + Red)}$$

$$MNDWI = \frac{(Green - SWIR\ 1)}{(Green + SWIR\ 1)}$$

$$(2)$$

$$SAVI = \frac{(NIR - Red) * 1.5}{(NIR + Red) + 0.5}$$

$$(3)$$

$$BI = \frac{(SWIR\ 1 + Red) - (NIR + Blue)}{(SWIR\ 1 + Red) + (NIR + Blue)}$$

$$(4)$$

$$UI = \frac{(SWIR\ 2 - NIR)}{(SWIR\ 2 + NIR)}$$

$$(5)$$

$$NDWI = \frac{(Green - NIR)}{(Green + NIR)}$$

$$(6)$$

$$NDBI = \frac{(SWIR\ 1 - NIR)}{(SWIR\ 1 + NIR)}$$

$$(7)$$

The beauty of these indices is also their power to discriminate objects while making their color composites. Different combinations yield different colors depending upon the number of available indices. Application of different spectral indices in the combination process maximizes the number of combinations yielding a distinct color for each feature class either in false or true colors easing visual interpretation and ultimately assisting machine learning for better feature recognition. From the eight spectral indices a total of 336 different color composites can be generated using the permutation formula as shown in Equation (9) for visualization. This is so because order of spectral indices while making the composites has an effect on the final color output depending on the amount of energy absorbed or reflected and the channel assigned to pursuant to the type of index chosen. However, according to our iterative experiment a satisfactory result was obtained when the compositing was made upon picking one index from the indices we grouped limiting the total number of combinations to 56, which were then used for the classification purpose.

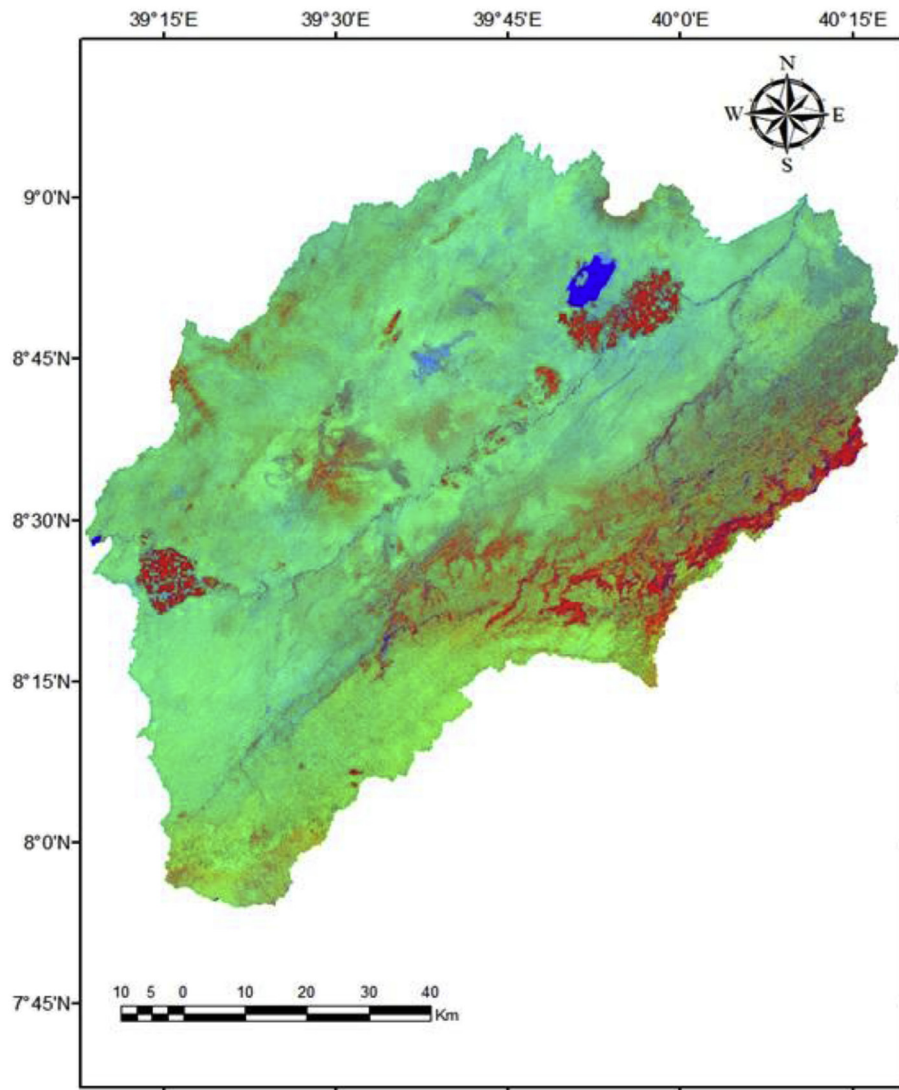


Fig. 9. Refined color composite of spectral indices with NDVI, NDBI and NDWI for the image extracted from the year 1995. (For interpretation of the references to color in this figure legend, the reader is referred to the Web version of this article.)

$$n_{Pr} = \frac{n!}{(n - r)!} \quad (9)$$

where n_{Pr} denotes the total number of permutation output, n is the total number of spectral indices (8 in this case), r is the number of spectral indices selected for compositing (3 in this case) and ! is the factorial notation.

Then indices signifying land features of similar or closer spectral behavior have been categorized into three distinct groups to optimally select three indices for compositing. The grouping process has also considered spectral similarity as tested by Pearson's correlation matrix taking 60 observations from individual class. Indices developed for a particular land cover type have closer affinity to each other with strong positive correlation value as shown in Table 9 and Fig. 8. The groups are: Group-1: (NDVI (Tucker, 1979) and SAVI (Huete, 1988)), Group-2: (CVUI (Wagner et al., 2012), BI (Rikimaru & Miyatake, 1997), UI (Assyakur et al., 2012) and NDBI (Zha et al., 2003)) and Group-3: (MNDWI (Xu, 2006) and NDWI (Gao, 1996)). Group-1 consists of indices developed to study vegetation properties and their distributions. Group-2 has indices dealing with bareness, soils, built-up and all developed infrastructures. Group-3 comprises of indices developed to study water resources distribution and their constituents. Even though CVUI was categorized under group-1 based on the target domain by the

developer, it didn't show closer affinity to the other classes, instead it inclined towards the water group. Therefore, we excluded it as a discriminant feature in our analysis.

Afterwards, a series of experiments have been carried out on index compositing to select a composite that best reflect the different land cover types. The experiments was based on spectral indices combination trials. The selected image for the experiment was the image of the year 2017 so that comparison of the combination output would be based on the reliable ground reference data we have. Then we started our experiment by making a series of combination trials crosschecking each result with the available higher resolution Google earth images, Baidu and Bing maps, and field survey records. Since each combination resulted in unique color, visibility and interpretability of different object varied accordingly. We ranked combinations based on the clarity of landmarks that we put on the ground reference data. All combination trials have yielded a relatively clear and smooth image showing that compositing indices in general is a viable option for coarse image classification process for example for easily identifiable land objects like water, vegetation and bare lands. However, a better output could be obtained when composite of three indices from each index group. One of the resulting composites can be represented by Fig. 9, which is a product of compositing NDVI from Group-1, NDBI from Group-2 and NDWI from Group-3. This compositing image resulted in partly a true

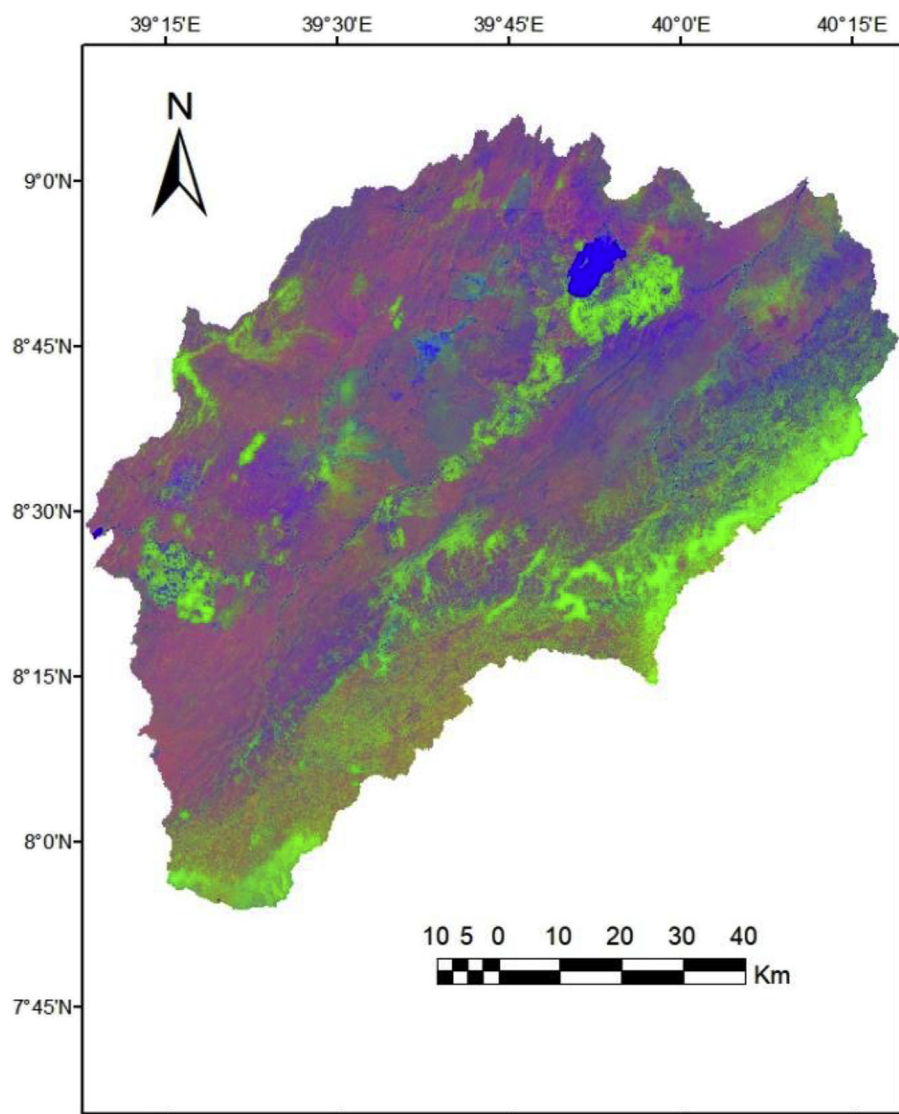


Fig. 10. Color composite of spectral indices with BI, NDVI and NDWI showing true color for vegetation and water for image extracted from year 2017. (For interpretation of the references to color in this figure legend, the reader is referred to the Web version of this article.)

color and partly a false color image depending on the type of indices used and their order of combination. Assigning NDVI to a red channel implies that the NIR is being applied to obtain the maximum reflectance yielding red color for vegetation. Similarly NDWI, which is a water index was assigned to blue channel and as a result a true blue color for water was obtained. Alternatively, a composite made up of BI, NDVI and NDWI with RGB order has yielded true color for green and blue channels where green vegetation and blue water could apparently be distinguished from the resulting image (Fig. 10).

3.6. Image classification and accuracy assessment

In the classification process we applied different methods depending on the quality of the extracted information from PCA and spectral indices. In our first attempt of classification, we have applied maximum likelihood algorithm imbedded in ENVI version 5.3. Maximum likelihood classification algorithm was chosen because it has been one of the popular supervised classification technique that maximizes the probability of a pixel to be grouped in the most similar neighboring class based on the pixel value of well refined training samples. The classification result based on the training samples from PCA and

Table 10
Mean value of spectral indices for each class calculated for the image of the year 2017.

Class	UI	SAVI	NDWI	NDVI	NDBI	MNDWI	CVUI	BI
Barren/developed land	-0.1010	0.0909	-0.1945	0.1901	-0.0003	-0.1934	-0.0226	-0.5462
Forest	-0.5367	0.2577	-0.4666	0.5361	-0.3059	-0.1820	-0.3015	-1.4259
Irrigated farmland	-0.6350	0.3618	-0.5295	0.5858	-0.3626	-0.1590	-0.3737	-1.2728
Rain-fed cropland	0.0424	0.1065	-0.2527	0.1746	0.1359	-0.3756	0.0071	-0.0626
Water bodies	-0.7292	-0.0639	0.2734	-0.1889	-0.6239	0.7774	0.1570	-1.9110
Wood/shrubland	-0.2689	0.1607	-0.3232	0.3148	-0.0657	-0.2626	-0.0903	-0.6254

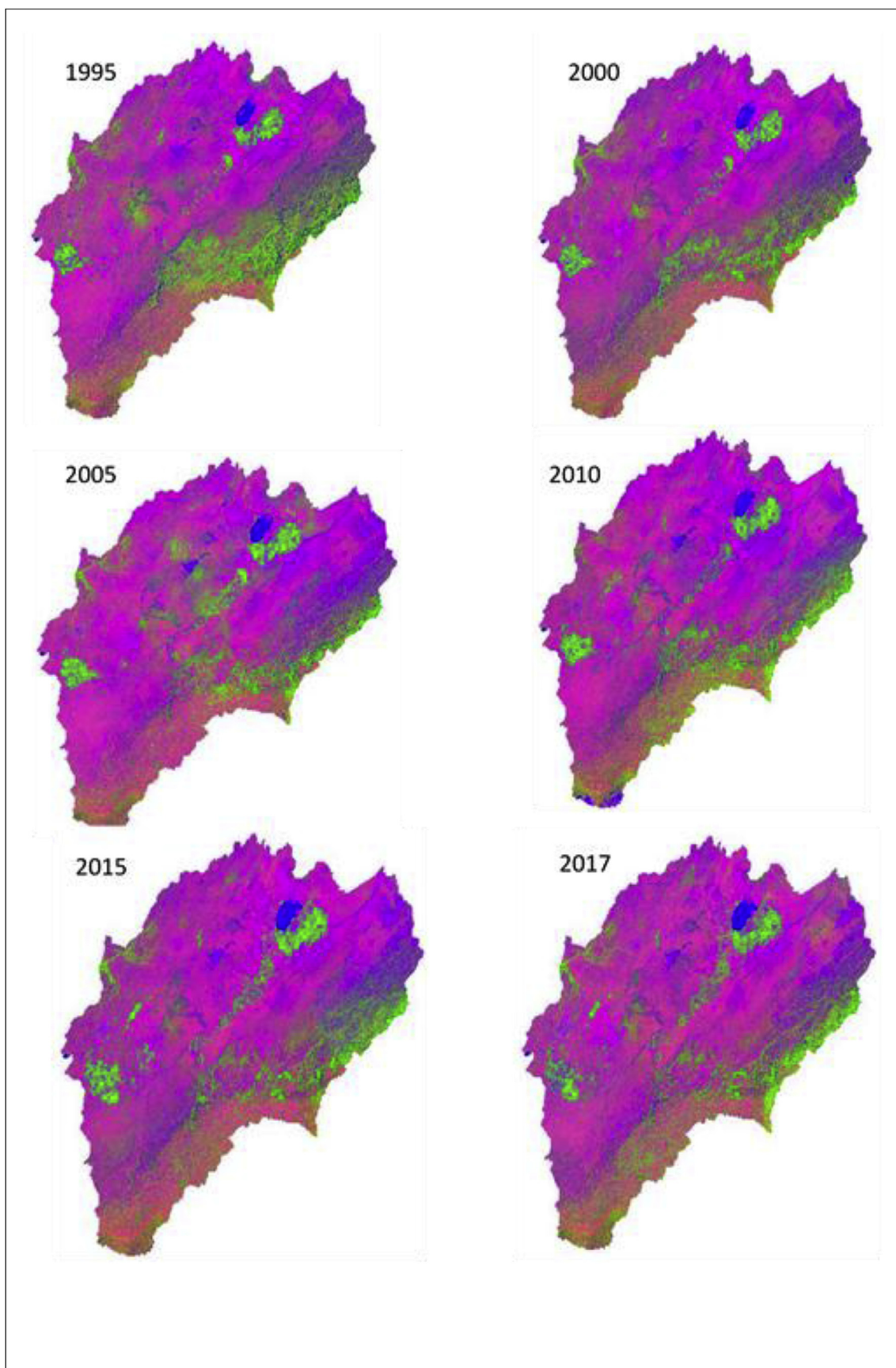


Fig. 11. Composites of spectral indices for the referenced years with NDBI, NDVI and NDWI with respective orders based on image of the year 2017.

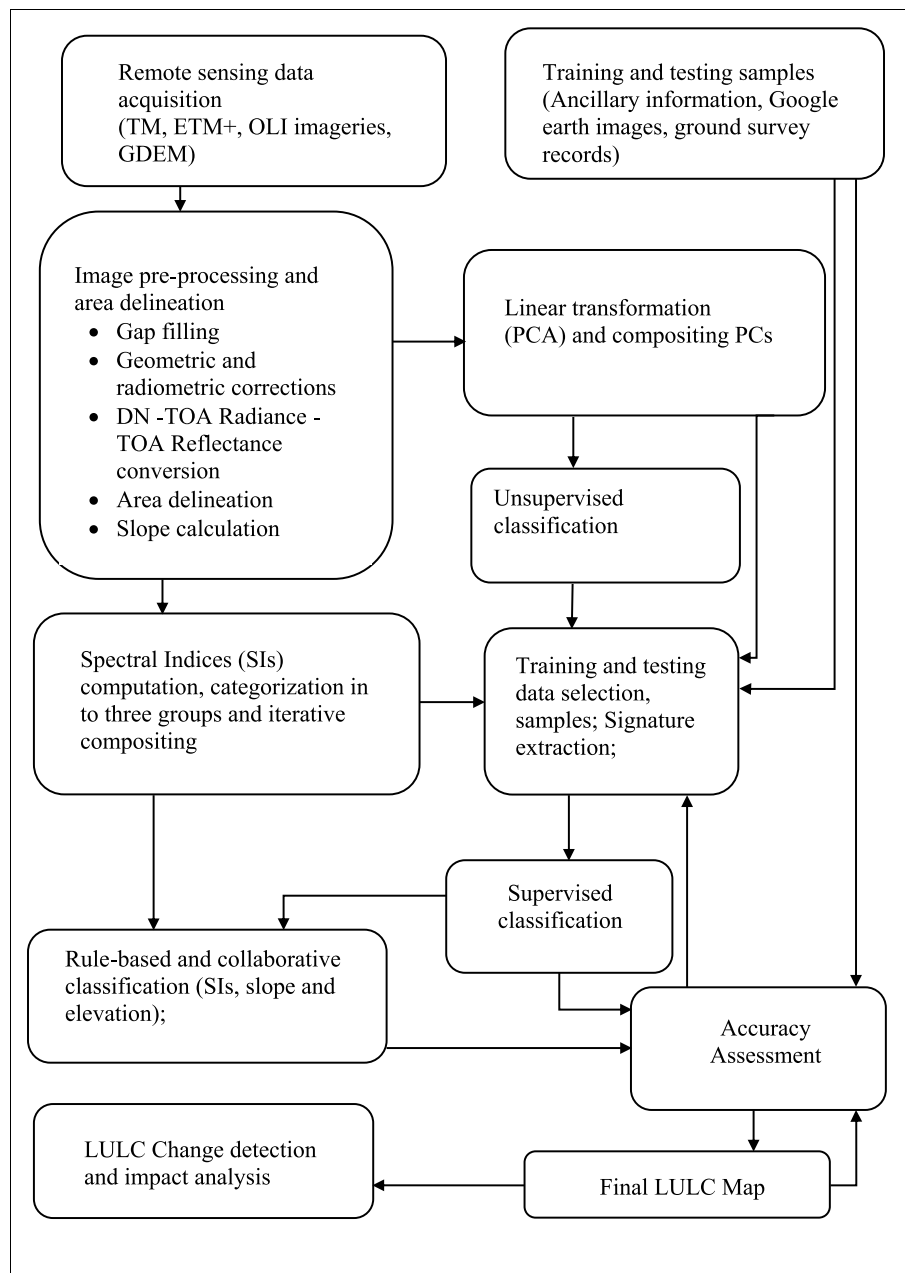


Fig. 12. Study methodology flow chart.

combination of spectral indices has enabled us to easily distinguish water body with small erroneously included land cover portion from other classes due to shadowing effect. The shadowing effect was observed at places where there were high landscape relief and, thus we applied here slope calculation and rule based classification to subtract the area occupied by those erroneously included pixel in water body class. Vegetated land cover was also traceable except the difficulty to spectrally distinguish irrigated farmland from forest. We managed to distinguish these two land features by integrating elevation and slope calculations using Boolean operator, where irrigated farmland occupying the gentle to plain part of the study area. This of course doesn't mean that there could not be forest land cover in gentle or plain area. Rather, this was a location specific instance where in the study area the forest cover was concentrated in the elevated and sloppy areas as proved from earlier maps (Ethiopia Land Cover, 2003, 2008, 2013 Scheme I and II maps produced by RCMD, Topographic map and ground survey). Wood/shrubland class has also showed closer spectral

value with irrigated farmland and forest classes, but its reflective capacity and spatial distribution has made it distinguishable from the other two classes as can be seen in Table 10. Specifically, the NDVI and SAVI values of Wood/shrubland were lower than that of forest and irrigated farmland because of the data collection period where spectral values decreased due to leaf shedding effect. Barren/developed land and rain-fed cropland have similarly shown very close spectral similarity during training sample selection, but the PCA has yielded a unique pinkish-brown color for harvested rain-fed cropland, which could be attributed to the high organic matter from crop residues, and thus it could easily be discriminated from barren/developed land.

We finally used the composites made of NDBI, NDVI and NDWI as an input file for classification for each year with RGB combination order respectively (Fig. 11). Similarly, the training and testing samples were taken from the composite of the individual year's image. The distribution of the training samples were based on the visible and clearly identifiable surface objects from the composited images, aided by

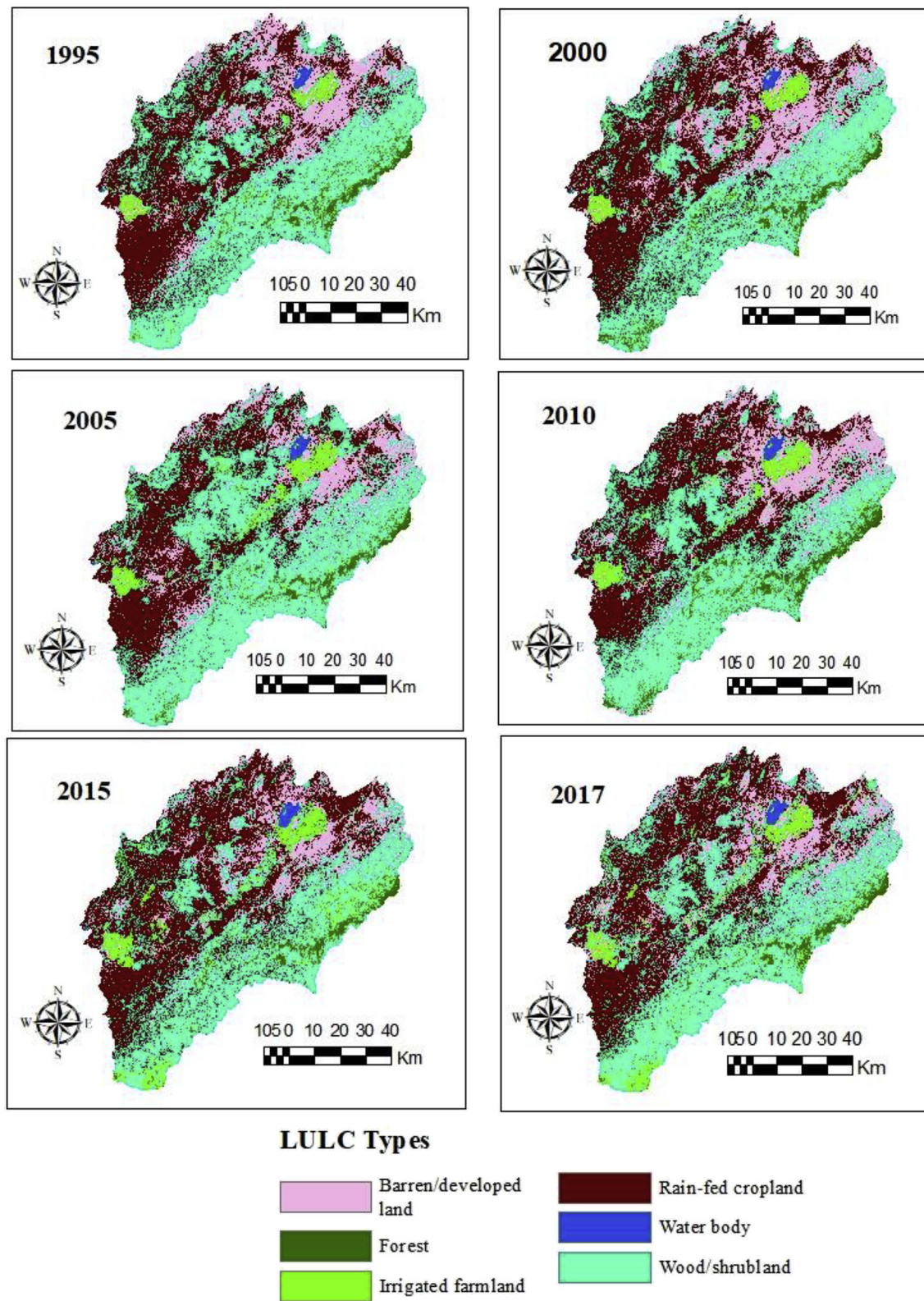


Fig. 13. Classified LULC maps for the years 1995, 2000, 2005, 2010, 2015 and 2017.

Google earth images, Baidu and Bing maps.

Because of the fact that all classification algorithms perform under probability of certain errors, it is a mandatory step to perform accuracy assessment based on ground reference data. In order to test the classification accuracy, therefore, we have followed the steps outlined by Feng et al. (2017). All considerations outlined by Congalton (1991) for

accuracy assessment, i.e. ground reference data collection, LULC classification scheme, autocorrelation, sample size and sampling scheme were taken while handling ground truths and ancillary data. Stratified random sampling was the base for the sampling method. The Guide book on sampling techniques by Cochran (1977) was reviewed for practical application of the sampling size in stratified random sampling

Table 11

Confusion matrix of LULC map produced from image of 2017.

Class	Barren/developed land	Forest	Irrigated farmland	Rain-fed cropland	Water body	Wood/shrubland
Barren/developed land	172	8	0	26	0	2
Forest	0	116	2	0	0	9
Irrigated farmland	0	3	68	0	0	6
Rain-fed cropland	16	0	0	220	0	0
Water body	0	0	0	0	65	0
Wood/shrubland	0	10	0	0	0	271
Producer accuracy	91.49	84.67	97.14	89.43	100	94.1
User accuracy	82.69	91.34	88.31	93.22	100	96.44
Overall accuracy			91.75%			
Kappa coefficient			0.89			

method.

However, ground verification was challenged by access, budget and time constraints. As it was suggested by Congalton (1991), we have reduced the sample size for the stratified random sampling process for smaller classes like water, forest and irrigated farmland without compromising the minimum number of samples (50), which he recommended as a rule of thumb. Among the distributed random samples in each class 70% was allocated for training and 30% for testing the accuracy. Accordingly, the image classification accuracy assessment was initially performed for the year 2017 using confusion matrix based on ground truthing points collected during the field survey campaign in 2017 and the corresponding classified image of the year with distributed random samples over the individual class and verifying the correctness by crosschecking the point along with high resolution Google earth images, Baidu and Bing maps. Random sample distributed in the classified maps were checked against data collected from Google earth, Baidu and Bing maps using Collect Earth. Although we have made accuracy assessment for the earlier years, we lack trust as high resolution satellite image or ancillary maps with better resolution other than the Landsat image could not be obtained. We have also reviewed the work of Olofsson, Foody, Stehman, and Woodcock (2013) to consider the incorporation of all accuracy assessment details. Performance indicators, i.e. overall accuracy, kappa coefficient, producer and user accuracy were calculated from the confusion matrix to determine

Table 12
LULC distribution over the study period.

LULC type	Area (Km ²)					
	1995	2000	2005	2010	2015	2017
Barren/developed land	1856.61	1952.40	1482.02	1709.95	1545.04	1688.72
Forest	376.07	368.85	371.64	528.61	346.32	328.97
Irrigated farmland	223.89	269.55	301.86	310.11	458.57	462.65
Rain-fed cropland	3166.74	3407.92	2805.60	3079.46	3664.09	3311.81
Water body	39.56	40.70	42.29	44.81	49.45	47.95
Wood/shrubland	3854.27	3477.73	4513.73	3844.20	3453.68	3677.05
Total	9517.1	9517.1	9517.1	9517.1	9517.1	9517.1

applicability of the classification method for further LULC dynamics and trend analysis.

The overall study process from data acquisition to the final LULC change analysis, was represented by schematic diagram shown in Fig. 12.

4. Results and discussion

4.1. LULC classification outputs and performance evaluation

The classification results were presented in (Fig. 13). Accuracy

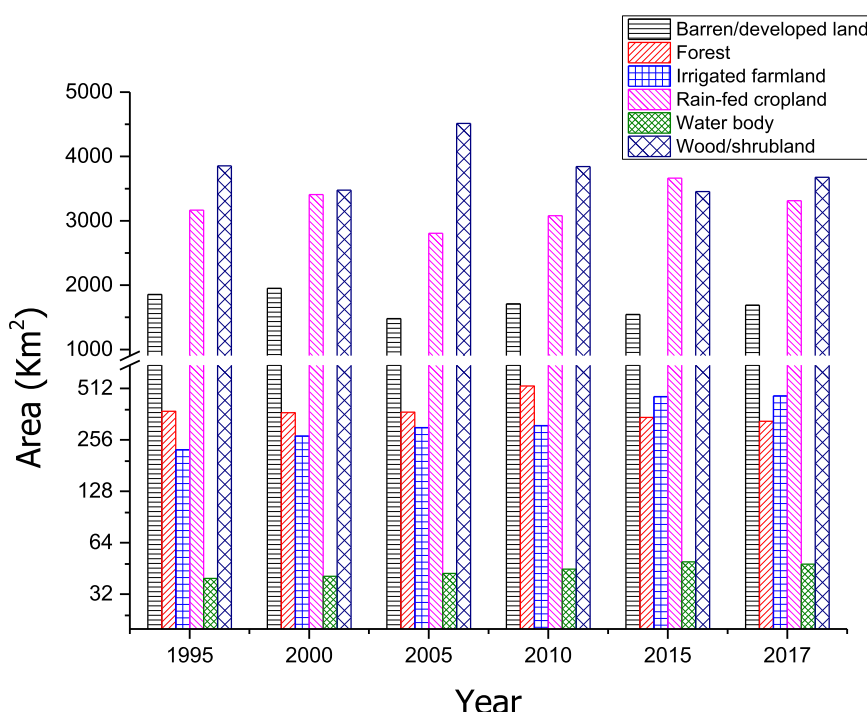
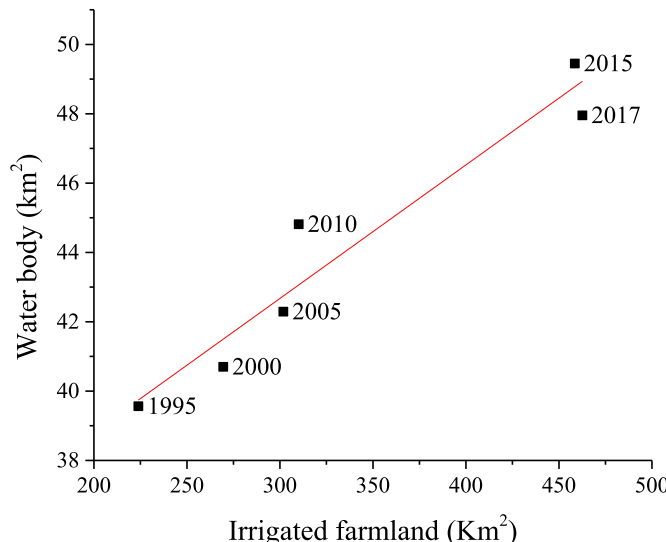
**Fig. 14.** LULC distribution and change trend in Middle Awash subbasin.

Table 13

Statistics computed from auto-coregistered images for area cover change from 1995 to 2017.

Class	Initial state (1995) area (Km ²)							
	Barren/developed land	Forest	Irrigated farmland	Rain-fed cropland	Water body	Wood/Shrub land	Row Total	
Final state (2017)area (Km ²)								
Unclassified	1.13	0.14	0.04	1.82	0.02	1.53	4.67	
Barren/developed land	735.79	11.04	34.33	360.67	1.14	544.85	1687.82	
Forest	2.87	203.27	14.11	5.16	0.89	102.48	328.79	
Irrigated farmland	72.29	19.12	110.04	79.6	0.75	180.65	462.45	
Rain-fed cropland	662.76	2.15	6.8	2128.48	0.07	509.46	3309.73	
Water body	6.34	0.48	1.08	1	36.1	2.92	47.93	
Wood/shrubland	375.44	139.87	57.49	590.02	0.57	2512.37	3675.75	
Class Total	1856.61	376.07	223.89	3166.74	39.56	3854.27	9517.14	
Class Changes	1120.82	172.8	113.85	1038.26	3.46	1341.9		
Image Difference	-168.79	-47.28	238.56	142.99	8.37	-178.52		

**Fig. 15.** Linear curve fit of irrigated farmland and water body from year 1995–2017.

performance evaluation was made based on the known performance indicators computed from the confusion matrix between the collected testing data, which were encoded as a point vector file and later converted to regions of interest with respect to the identified classes and the classified image of the year 2017. Accordingly, a satisfactory accuracy with an overall accuracy of 91.75% (912/994 pixels) and kappa coefficient of 0.89 was obtained. The producer and user accuracy for individual class is presented in Table 11. The result, therefore, assures the acceptability of post classification analysis.

4.2. LULC change detection, trend analysis and environmental implications

Middle Awash subbasin has undergone a dynamic changes since 1995 to 2017 (Fig. 14.). The distribution and areal coverage of all classes across the study periods is indicated in Table 12 and the overall change from the starting year (1995) to the final year (2017) is presented in Table 13. The subbasin was dominantly covered by wood/shrub land and rain-fed cropland with average land cover of 40% and 34% respectively, followed by barren/developed land covering about 18% of the study area. The rest was covered by forest, irrigated farmland and water body accounting for 4.1%, 3.5% and 0.5% respectively. According to the change detection result irrigated farmland, water body and rain-fed cropland have increased by 106.6%, 21.1% and 4.5% respectively. On the other hand forest, barren/developed land and wood/shrubland decreased by 12.6%, 9.1% and 4.6% respectively. A number of drivers could be mentioned for the causes of changes. Among

which anthropogenic activities took the major part, which was manifested by the rapid development of irrigation practices for commercial crops and decreased forest cover attributed to encroachment of local people for timber and firewood.

A sinusoidal pattern of change was observed in forest cover with a sign of declining trend from 1995 to 2000 followed by an increasing trend to its pick in 2010 and finally gradual decrease until 2017. This might be related to clearing of forest followed by regeneration. Regeneration is a gradual change requiring several years to be spectrally discriminated from the surrounding vegetation (Van Den Hoek, Ozdogan, Burnicki, & Zhu, 2014). The inter-annual changes observed in barren/developed and woodland/shrubland could be linked to the temporal and spatial variations in temperature and rainfall patterns. As we analyzed the meteorological data of Abomsa, Awash 7 kilo, Huruta, Metehara, Nuraera and Nazeret stations obtained from National Meteorological Agency of Ethiopia, there have been seasonal and annual variations of temperature and precipitation in the study area throughout the entire study period. These variations could affect agricultural activities and phenological properties causing changes in spectral signatures of land covers. Land cover changes could also be affected by wildfires, grazing and reachability of the area by animals for instance due to slope and aspect (Jucker Riva, Daliakopoulos, Eckert, Hodel, & Liniger, 2017). Nevertheless, detailed investigation through regular monitoring scheme is compulsory to fully capture the general change situation.

Along with these changes, the hot environmental issue of the sub-basin is the rapidly expanding saline Lake Beseka (Dinka, 2017). The Lake takes the biggest share among the existing water bodies (e.g. 97% in 2017) and has become a major threat to the productive agricultural land around its periphery. It has been showing a scary trend of expansion having positive correlation ($r = 0.97$, adjusted $r = 0.92$) with expansion of irrigated farmland (Fig. 15, Fig. 16). The trend relationship between irrigated farmland and water bodies can be approximated by the equation:

$$y = 31.12 + 0.039x \quad (10)$$

where y denotes the areal coverage of the total water bodies and x represents the total irrigated farmland size in the study area both in square kilometers.

Based on the extracted shape file from aerial photo taken in 1972, the Lake area was found to be 11.7 km². On the other hand, the areal coverage in 2005 and 2017 as delineated from the classified water bodies was estimated at 41.1 km² and 46.7 km² respectively, which accounts for a total increment of about 35 km² since 1972. Despite its positive impact in diluting and increasing water availability potential, it is currently accompanied by numerous negative environmental consequences. It has to be noted that almost all of the people living in and around the main Awash River Basin in one way or another are dependent upon the perennial fresh Awash River. The rise in water level of Lake Beseka, has a possibility of

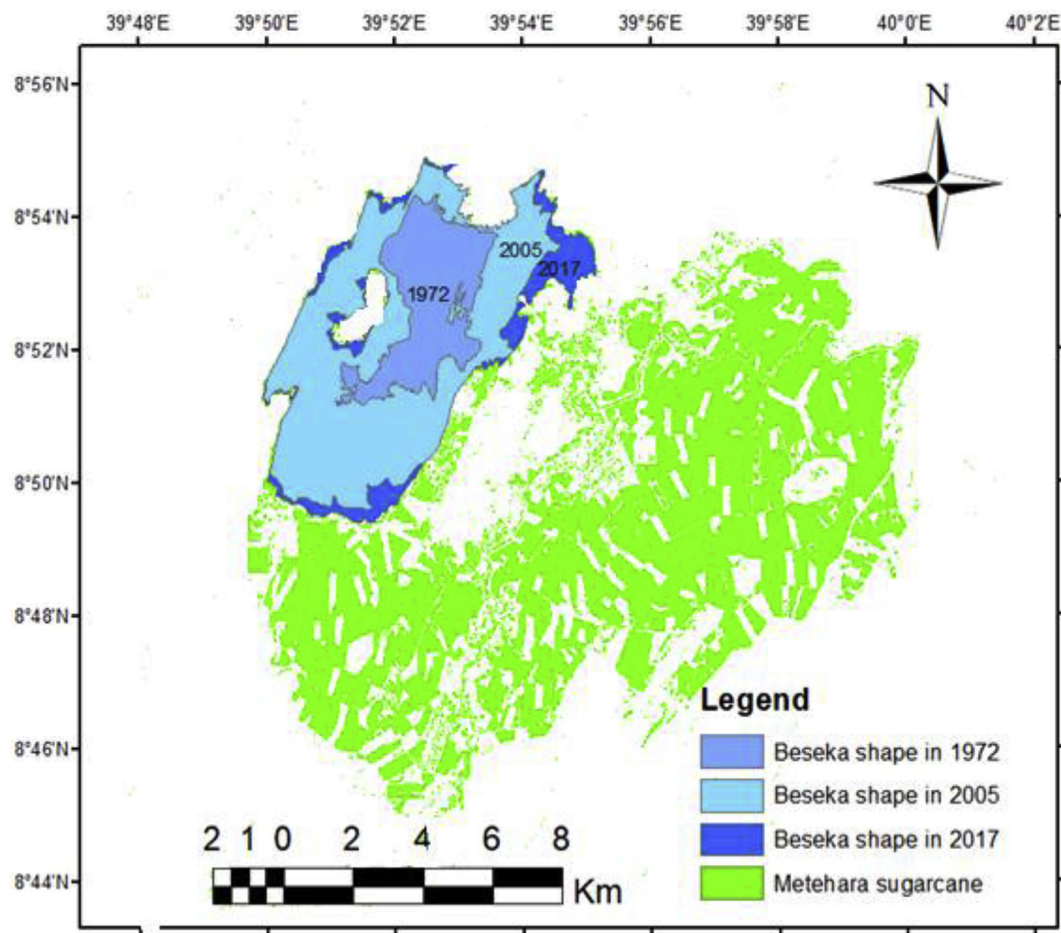


Fig. 16. Overlay of Lake Beseka polygon showing incremental trend from year 1972–2017 and the surrounding Metehara sugarcane plantation mapped from 2017 OLI image.

crossing the natural boundary of the closed system and contaminating this fresh water source besides the progressive inundation of the town dwellers property and the observed salinization effect on the neighboring fertile irrigated farmland. This situation is a serious threat to the socio-economic stability of the entire basin and thus, requires regular monitoring plan and appropriate management system. As a first step of tackling the problem, Ministry of Water, Irrigation and Electricity of Ethiopia and Awash Basin authority have tried to control the lake water level since 2015 by excavating a canal and discharging the water into Awash River in a regulated manner. The effect of intervention was clearly observed from the classified maps, where shrinkage of water body was observed in 2017 as compared to that of 2015. The sustainability and effectiveness of the counteractive measure has, however, not been evaluated yet, which should be addressed by regular monitoring effort. Other optional management measures like introduction of modern irrigation technologies have not been exhaustively considered either. In this regard, land managers should consider the incorporation of suitability of irrigation methods as an additional factor to those outlined by Worqlul et al. (2017) for identifying suitable area for surface irrigation: physical land features, climate and market facilities. In general terms, rural land suitability map should be prepared based on suitability ranks considering physical status of the land, socio-economic status and rural development trends, which could be generated by integrating analytical hierarchy process (AHP), GIS and multiple criteria decision analysis (Liu, Tang, Liu, Zhao, & He, 2017a).

5. Conclusions

Monitoring LULC changes in a spectrally heterogeneous

environment is the most challenging task in the current remotely sensed data-based analysis process. This situation has challenged the threshold-based image classification process. In this study, we have made a detailed experiment on how to improve image classification accuracy by integrating principal component analysis and composites of spectral indices. PCA and composites of spectral indices, augmented by ground survey and ancillary data have greatly assisted to accurately trace training samples for machine learning. PCA has played a great role in reducing spectral dimensionality, which helped to easily extract signatures of land features. Similarly, composites of spectral indices have showed an interesting capacity of yielding visually clear distinct colors, which helped to discriminate the different land features, particularly water, vegetated land covers and barren lands without putting much effort. This result is particularly important to monitor expansion of small lakes and reservoirs, so that appropriate corrective measures can be taken at the right time, which may otherwise have a significant impact on the surrounding. The saline Lake Beseka, which has been continuously expanding and creating threat to the livelihood of the local people, their water resource and productive land is a typical example that requires regular monitoring and corrective measures. The classification method is also effective to monitor vegetation distribution and its health as it sensitively discriminates chlorophyll content.

Despite these merits there are still challenges of discriminating land features under shadow cover. It has also limitations on isolating different land features lumped under barren/developed land cover. It is, therefore, important to augment these techniques with scheduled ground survey and high spatial resolution images for better classification accuracy.

In the case study, we have identified and successfully classified six major LULC classes of the subbasin using the proposed techniques. Wood/shrubland and rain-fed cropland were the dominant land covers across all the study periods followed by barren/developed land, forest, irrigated farmland and water body respectively. From the image classification and change detection results we could clearly notice that the subbasin has undergone a dynamic change in LULC. A remarkable correlation was observed on expansion of irrigation farmland and water body with an adjusted R-Square of 0.92. Continuous increase in water body was mainly attributed to the expansion of the saline Lake Beseka, which took the biggest proportion among the existing water body constituents and believed to be caused by irrigation return flow. A continuous decrease in the electrical conductivity and total dissolved solids of the Lake water is a clue for the addition of fresh water to the Lake from irrigation return flow. On the other hand, a sinusoidal pattern of change was observed in forest cover with a sign of declining trend from 1995 to 2000 followed by an increasing trend to its pick in 2010 and finally gradual decrease until 2017. The sinusoidal pattern could be linked to the clearing of forest followed by regeneration. The overall change, however, signifies a declining trend, which could be associated with socio-economic drivers though it requires detailed study to attest the presumption.

In general, this study has showed that remote sensing and GIS are key tools to monitor LULC changes. It was proven that any piece of remote sensing data is highly valuable so long as different study approaches are experimented to extract useful information from raw data. It was witnessed by the improvement of classification accuracy, which was achieved by augmenting principal component analysis with composites of spectral indices. In due course the study could highlight the LULC status and dynamics of the study area, which could serve as a starting point for further trend analysis, policy formulation and future land use planning.

Declaration of interest

None.

Acknowledgements

This research was supported by project No. 2016YFE0115800 funded by Joint Innovative and Technological Research Projects from Ministry of Science and Technology of the People's Republic of China and project No. PCRRIC16005 by the State Key Laboratory of Pollution Control and Resource Reuse of Tongji University. The authors would also acknowledge Ministry of Commerce of People Republic of China and UN-Environment-Tongji Institute of Environment for Sustainable Development (IESD) for laying a conducive environment to the first author to carry out this research. Last but not least, the constructive comments and advices of the anonymous reviewers greatly improved the work and thus we would like to extend our appreciation.

References

- Abd El-Kawy, O. R., Rød, J. K., Ismail, H. A., & Suliman, A. S. (2011). Land use and land cover change detection in the western Nile delta of Egypt using remote sensing data. *Applied Geography*, 31, 483–494.
- Abdulaziz, A. M., Hurtado, J. J. M., & Al-Douri, R. (2009). Application of multitemporal Landsat data to monitor land cover changes in the Eastern Nile Delta region, Egypt. *International Journal of Remote Sensing*, 30, 2977–2996.
- Akhtar, F., Awan, U. K., Tischbein, B., & Liaqat, U. W. (2017). A phenology based geoinformatics approach to map land use and land cover (2003–2013) by spatial segregation of large heterogenic river basins. *Applied Geography*, 88, 48–61.
- Alphan, H., Doygun, H., & Unlukaplan, Y. I. (2009). Post-classification comparison of land cover using multitemporal landsat and ASTER imagery: The case of Kahramanmaraş, Turkey. *Environmental Monitoring and Assessment*, 151, 327–336.
- Anderson, J. R., Hardy, E. E., Roach, J. T., & Witmer, R. E. (2001). *A land use and land cover classification system for use with remote sensor data*. Washington: US Government Printing Office First Printing Geological survey professional paper 964.
- Ariti, A. T., van Vliet, J., & Verburg, P. H. (2015). Land-use and land-cover changes in the Central Rift Valley of Ethiopia: Assessment of perception and adaptation of stakeholders. *Applied Geography*, 65, 28–37.
- As-syakur, A. R., Adnyana, I. W. S., Arthana, I. W., & Nuarsa, I. W. (2012). Enhanced built-up and bareness index (EBBI) for mapping built-up and bare land in an urban area. *Remote Sensing*, 4, 2957–2970.
- Bao, A., Huang, Y., Ma, Y., Guo, H., & Wang, Y. (2017). Assessing the effect of EWDP on vegetation restoration by remote sensing in the lower reaches of Tarim River. *Ecological Indicators*, 74, 261–275.
- Biazin, B., & Sterk, G. (2013). Drought vulnerability drives land-use and land cover changes in the Rift Valley dry lands of Ethiopia. *Agriculture, Ecosystems & Environment*, 164, 100–113.
- Brenner, J. C., Christman, Z., & Rogan, J. (2012). Segmentation of landsat thematic mapper imagery improves buffelgrass (*pennisetum ciliare*) pasture mapping in the Sonoran desert of Mexico. *Applied Geography*, 34, 569–575.
- Brunori, E., Salvati, L., Mancinelli, R., Smiraglia, D., & Biasi, R. (2016). Multi-temporal land use and cover changing analysis: The environmental impact in Mediterranean area. *The International Journal of Sustainable Development and World Ecology*, 24, 276–288.
- Chander, G., Markham, B. L., & Helder, D. L. (2009). Summary of current radiometric calibration coefficients for Landsat MSS, TM, ETM+, and EO-1 ALI sensors. *Remote Sensing of Environment*, 113, 893–903.
- Chen, Z. M., Babiker, I. S., Chen, Z. X., Komaki, K., Mohamed, M. A. A., & Kato, K. (2004). Estimation of interannual variation in productivity of global vegetation using NDVI data. *International Journal of Remote Sensing*, 25, 3139–3159.
- Chen, X.-L., Zhao, H.-M., Li, P.-X., & Yin, Z.-Y. (2006). Remote sensing image-based analysis of the relationship between urban heat island and land use/cover changes. *Remote Sensing of Environment*, 104, 133–146.
- Cochran, W. G. (1977). *Sampling techniques*. New York: John Wiley & Sons.
- Congalton, R. G. (1991). A review of assessing the accuracy of classifications of remotely sensed data. *Remote Sensing of Environment*, 37, 35–46.
- Coppin, P., Jonckheere, I., Nackaerts, K., Muys, B., & Lambin, E. (2004). Review article digital change detection methods in ecosystem monitoring: A review. *International Journal of Remote Sensing*, 25, 1565–1596.
- Deepa, P., & Thilagavathi, K. (2015). Feature extraction of hyperspectral image using principal component analysis and folded-principal component analysis. *2015 2ND international conference on electronics and communication system (ICECS 2015)* (pp. 656–660). Coimbatore, India: IEEE.
- Ding, K., Chen, S., & Meng, F. (2018). A novel perceptual hash algorithm for multispectral image authentication. *Algorithms*, 11, 6.
- Dinka, M. O. (2017). Lake Basaka Expansion: Challenges for the sustainability of the matahara irrigation scheme, Awash River basin (Ethiopia). *Irrigation and Drainage*, 66, 305–315.
- Dinka, M. O., Loiskandl, W., & Ndambuki, J. M. (2015). Hydrochemical characterization of various surface water and groundwater resources available in Matahara areas, Fantalle Woreda of Oromiya region. *Journal of Hydrology: Regional Studies*, 3, 444–456.
- Feng, Y., Lu, D., Moran, E., Dutra, L., Calvi, M., & de Oliveira, M. (2017). Examining spatial distribution and dynamic change of urban land covers in the Brazilian Amazon using multitemporal multisensor high spatial resolution satellite imagery. *Remote Sensing*, 9, 381.
- Galvani, A. P., Bauch, C. T., Anand, M., Singer, B. H., & Levin, S. A. (2016). Human–environment interactions in population and ecosystem health. *Proceedings of the National Academy of Sciences*, 113, 14502–14506.
- Ganbold, G., & Chasila, S. (2017). Comparison between possibilistic c-means (PCM) and artificial neural network (ANN) classification algorithms in land use/land cover classification. *International Journal of Knowledge Content Development & Technology*, 7, 57–78.
- Gao, B.-C. (1996). NDWI-a normalized difference water index for remote sensing of vegetation liquid water from space. *Remote Sensing of Environment*, 58, 257–266.
- Gao, F., Anderson, M. C., Zhang, X., Yang, Z., Alfieri, J. G., Kustas, W. P., et al. (2017). Toward mapping crop progress at field scales through fusion of Landsat and MODIS imagery. *Remote Sensing of Environment*, 188, 9–25.
- Gebrehiwot, T., & van der Veen, A. (2014). Coping with food insecurity on a micro-scale: Evidence from Ethiopian rural households. *Ecology of Food and Nutrition*, 53, 214–240.
- Goodwin, N. R., Collett, L. J., Denham, R. J., Flood, N., & Tindall, D. (2013). Cloud and cloud shadow screening across Queensland, Australia: An automated method for Landsat TM/ETM+ time series. *Remote Sensing of Environment*, 134, 50–65.
- He, C., Shi, P., Xie, D., & Zhao, Y. (2010). Improving the normalized difference built-up index to map urban built-up areas using a semiautomatic segmentation approach. *Remote Sensing Letters*, 1, 213–221.
- Hilker, T., Wulder, M. A., Coops, N. C., Linke, J., McDermid, G., Masek, J. G., et al. (2009). A new data fusion model for high spatial- and temporal-resolution mapping of forest disturbance based on Landsat and MODIS. *Remote Sensing of Environment*, 113, 1613–1627.
- Huang, C., Song, K., Kim, S., Townshend, J. R. G., Davis, P., Masek, J. G., et al. (2008). Use of a dark object concept and support vector machines to automate forest cover change analysis. *Remote Sensing of Environment*, 112, 970–985.
- Huete, A. R. (1988). A soil-adjusted vegetation index (SAVI). *Remote Sensing of Environment*, 25, 295–309.
- Jimenez, L. O., & Landgrebe, D. A. (1999). Hyperspectral data analysis and supervised feature reduction via projection pursuit. *IEEE Transactions on Geoscience and Remote Sensing*, 37, 2653–2667.
- Jin, S., Yang, L., Zhu, Z., & Homer, C. (2017). A land cover change detection and classification protocol for updating Alaska NLCD 2001 to 2011. *Remote Sensing of Environment*, 195, 44–55.

- Jucker Riva, M., Daliakopoulos, I. N., Eckert, S., Hodel, E., & Liniger, H. (2017). Assessment of land degradation in Mediterranean forests and grazing lands using a landscape unit approach and the normalized difference vegetation index. *Applied Geography*, 86, 8–21.
- Kamh, S., Ashmawy, M., Kilias, A., & Christaras, B. (2012). Evaluating urban land cover change in the Hurghada area, Egypt, by using GIS and remote sensing. *International Journal of Remote Sensing*, 33, 41–68.
- Kindu, M., Schneider, T., Teketay, D., & Knoke, T. (2015). Drivers of land use/land cover changes in Munessa-Shashemene landscape of the south-central highlands of Ethiopia. *Environmental Monitoring and Assessment*, 187, 452.
- Lambin, E. F., & Meyfroidt, P. (2011). Global land use change, economic globalization, and the looming land scarcity. *Proceedings of the National Academy of Sciences of the U.S.A.*, 108, 3465–3472.
- Liu, J., Hertel, T. W., Lammers, R. B., Prusevich, A., Baldos, U. L. C., Grogan, D. S., et al. (2017b). Achieving sustainable irrigation water withdrawals: Global impacts on food security and land use. *Environmental Research Letters*, 12, 104009.
- Liu, D., Tang, W., Liu, Y., Zhao, X., & He, J. (2017a). Optimal rural land use allocation in central China: Linking the effect of spatiotemporal patterns and policy interventions. *Applied Geography*, 86, 165–182.
- Li, H., Wang, C., Zhong, C., Su, A., Xiong, C., Wang, J., et al. (2017). Mapping urban bare land automatically from landsat imagery with a simple index. *Remote Sensing*, 9, 249.
- Maxwell, A. E., & Warner, T. A. (2015). Differentiating mine-reclaimed grasslands from spectrally similar land cover using terrain variables and object-based machine learning classification. *International Journal of Remote Sensing*, 36, 4384–4410.
- McFeeters, S. K. (1996). The use of the Normalized Difference Water Index (NDWI) in the delineation of open water features. *International Journal of Remote Sensing*, 17, 1425–1432.
- Mello, M. P., Vieira, C. A. O., Rudorff, B. F. T., Aplin, P., Santos, R. D. C., & Aguiar, D. A. (2013). Stars: A new method for multitemporal remote sensing. *IEEE Transactions on Geoscience and Remote Sensing*, 51, 1897–1913.
- Michel, U., He, L., Dong, G., Wang, W.-M., Yang, L., Liang, H., et al. (2013). Object-based change detection in rapid urbanization regions with remotely sensed observations: A case study of Shenzhen, China. 8893, 88931W.
- Mushore, T. D., Mutanga, O., Odindi, J., & Dube, T. (2016). Assessing the potential of integrated Landsat 8 thermal bands, with the traditional reflective bands and derived vegetation indices in classifying urban landscapes. *Geocarto International*, 32, 886–899.
- Novelli, A., Tarantino, E., Caradonna, G., Apollonio, C., Balacco, G., & Piccinni, F. (2016). Improving the ANN classification accuracy of landsat data through spectral indices and linear transformations (PCA and TCT) aimed at LU/LC monitoring of a river basin. In O. Gervasi, B. Murgante, S. Misra, A. M. A. C. Rocha, C. M. Torre, & D. Taniar, (Eds.). *International conference on computational science and its applications-ICCSA 2016* (pp. 420–432). Beijing, China: Springer International Publishing.
- Olofsson, P., Foody, G. M., Stehman, S. V., & Woodcock, C. E. (2013). Making better use of accuracy data in land change studies: Estimating accuracy and area and quantifying uncertainty using stratified estimation. *Remote Sensing of Environment*, 129, 122–131.
- Pathak, S. (2014). New Change Detection Techniques to monitor land cover dynamics in mine environment. *ISPRS - International Archives of the Photogrammetry, Remote Sensing and Spatial Information Sciences*, XL-8, 875–879.
- Qu, J., Li, Y., & Dong, W. (2018). Guided filter and principal component analysis hybrid method for hyperspectral pansharpening. *Journal of Applied Remote Sensing*, 12, 1.
- Rikimaru, A., & Miyatake, S. (1997). Development of forest canopy density mapping and monitoring model using indices of vegetation, bare soil and shadow. *Proceeding of the 18th Asian conference on remote sensing* Kuala Lumpur, Malaysia: ACRS.
- Roy, D. P., Zhang, H. K., Ju, J., Gomez-Dans, J. L., Lewis, P. E., Schaaf, C. B., et al. (2016). A general method to normalize Landsat reflectance data to nadir BRDF adjusted reflectance. *Remote Sensing of Environment*, 176, 255–271.
- Sieber, A., Kuemmerle, T., Prishchepov, A. V., Wendland, K. J., Baumann, M., Radloff, V. C., et al. (2013). Landsat-based mapping of post-Soviet land-use change to assess the effectiveness of the Oksky and Mordovsky protected areas in European Russia. *Remote Sensing of Environment*, 133, 38–51.
- Sun, Z.-L., Huang, D.-S., Cheung, Y.-M., Liu, J., & Huang, G.-B. (2005). Using FCMC, FVS, and PCA techniques for feature extraction of multispectral images. *IEEE Geoscience and Remote Sensing Letters*, 2, 108–112.
- Tucker, C. J. (1979). Red and photographic infrared linear combinations for monitoring vegetation. *Remote Sensing of Environment*, 8, 127–150.
- Van Den Hoek, J., Ozdogan, M., Burnicki, A., & Zhu, A. X. (2014). Evaluating forest policy implementation effectiveness with a cross-scale remote sensing analysis in a priority conservation area of Southwest China. *Applied Geography*, 47, 177–189.
- Vogelmann, J. E., Gallant, A. L., Shi, H., & Zhu, Z. (2016). Perspectives on monitoring gradual change across the continuity of Landsat sensors using time-series data. *Remote Sensing of Environment*, 185, 258–270.
- Wagner, M. A., Myint, S. W., & Cerveny, R. S. (2012). Geospatial assessment of recovery rates following a Tornado disaster. *IEEE Transactions on Geoscience and Remote Sensing*, 50, 4313–4322.
- Warner, K., Hamza, M., Oliver-Smith, A., Renaud, F., & Julca, A. (2009). Climate change, environmental degradation and migration. *Natural Hazards*, 55, 689–715.
- Woldegabriel, G., Aronson, J. L., & Walter, R. C. (1990). Geology, geochronology, and rift basin development in the central sector of the Main Ethiopia Rift. *The Geological Society of America Bulletin*, 102, 439–458.
- Wondie, M., Schneider, W., Melesse, A. M., & Teketay, D. (2011). Spatial and temporal land cover changes in the simen mountains national park, a world heritage site in Northwestern Ethiopia. *Remote Sensing*, 3, 752–766.
- Worqlul, A. W., Jeong, J., Dile, Y. T., Osorio, J., Schmitter, P., Gerik, T., et al. (2017). Assessing potential land suitable for surface irrigation using groundwater in Ethiopia. *Applied Geography*, 85, 1–13.
- Wulder, M. A., White, J. C., Goward, S. N., Masek, J. G., Irons, J. R., Herold, M., et al. (2008). Landsat continuity: Issues and opportunities for land cover monitoring. *Remote Sensing of Environment*, 112, 955–969.
- Xu, H. (2006). Modification of normalised difference water index (NDWI) to enhance open water features in remotely sensed imagery. *International Journal of Remote Sensing*, 27, 3025–3033.
- Xu, C., Gao, S., & Li, M. (2017). A novel PCA-based microstructure descriptor for heterogeneous material design. *Computational Materials Science*, 130, 39–49.
- Zabalza, J., Ren, J., Yang, M., Zhang, Y., Wang, J., Marshall, S., et al. (2014). Novel Folded-PCA for improved feature extraction and data reduction with hyperspectral imaging and SAR in remote sensing. *ISPRS Journal of Photogrammetry and Remote Sensing*, 93, 112–122.
- Zha, Y., Gao, J., & Ni, S. (2003). Use of normalized difference built-up index in automatically mapping urban areas from TM imagery. *International Journal of Remote Sensing*, 24, 583–594.
- Zhou, H., Jiang, H., Zhou, G., Song, X., Yu, S., Chang, J., et al. (2010). Monitoring the change of urban wetland using high spatial resolution remote sensing data. *International Journal of Remote Sensing*, 31, 1717–1731.
- Zhu, Z., Fu, Y., Woodcock, C. E., Olofsson, P., Vogelmann, J. E., Holden, C., et al. (2016). Including land cover change in analysis of greenness trends using all available landsat 5, 7, and 8 images: A case study from Guangzhou, China (2000–2014). *Remote Sensing of Environment*, 185, 243–257.